



Basketballspielen mit antropomorphen Robotern

Diplomarbeit

Kai Krieger



DIPLOMARBEIT
BASKETBALLSPIELEN
MIT ANTROPOMORPHEN ROBOTERN

Freigabe:

Der Bearbeiter:

Unterschriften

Kai Krieger



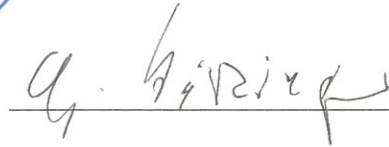
Betreuer:

Dipl. Ing., MSc. Sami Haddadin



Der Institutsdirektor

Prof. Dr. G. Hirzinger



Dieser Bericht enthält 82 Seiten und 35 Abbildungen

BASKETBALLSPIELEN MIT ANTROPOMORHPEN ROBOTERN

eingereichte
Diplomarbeit
von

cand. ing. Kai Krieger

geb. am 5.1.1984
wohnhaft in:
J.F. Weishaarstr.47
71404 Korb
Tel.: 0170 23407521

Institut für Robotik und Mechatronik
Deutsches Zentrum für Luft- und Raumfahrt (DLR e.V.)
Münchner Strasse 20
82234 Wessling

Professor Dr.-Ing. Gerd Hirzinger

Institut für Systemtheorie und Regelungstechnik (IST)
Universität Stuttgart
Pfaffenwaldring 9
70550 Stuttgart

Professor Dr.-Ing. Frank Allgöwer

Betreuer: Dipl. Ing., M.Sc. Sami Haddadin (DLR)
Dipl.-Ing. Christoph Maier (IST)
Beginn: 6. Oktober 2010
Abgabe: 29. April 2011

Abstract

For creating robots that are capable of human like performance in terms of speed, energetic properties, and robustness, intrinsic compliance is a promising design element for achieving this. In this thesis we investigate its capabilities referring to robot basketball dribbling. As for this task the ball can only be controlled during contact phase, an elastic hand mounted on a manipulator extends the contact time of the process. This also implicates the advantage of storing potential energy during contact and releasing it at beneficial time instances. We present the analysis and experimental validation with a seven degree of freedom Cartesian impedance controlled DLR lightweight robot for the stability and the control of this task. This work serves also as a preliminary investigation for the new DLR Hand Arm System. As a human is able to dribble blindly, we decided to develop a ball observer that takes only the measured contact forces into account, i.e. no vision system is needed for our approach.

Zusammenfassung

Ein vielversprechender Ansatz im Roboterdesign der es voraussichtlich erlaubt in Bereichen wie Geschwindigkeit, energetischen Eigenschaften und Robustheit ähnliche gute Leistungen wie ein Mensch erbringen zu können, ist intrinsische Nachgiebigkeiten im Gelenkdesign zu verwenden. Diese Eigenschaft wird in der vorliegenden Arbeit mit Bezug auf Roboter Basketball untersucht. Da der Ball dabei nur während der kurzen Kontaktphase beeinflusst werden kann, wird eine elastische Hand zur Verlängerung der Kontaktzeit verwendet. Diese Elastizität bietet ausserdem den Vorteil, dass potentielle Energie während des Kontaktes zwischengespeichert werden kann. Dafür werden in dieser Arbeit Analysen der Stabilität und der Regelung dieses Prozesses, sowie eine experimentelle Validierung mit einem DLR Leichtbauroboter mit sieben Freiheitsgraden präsentiert. Diese Arbeit dient insbesondere auch als Voruntersuchung für das neue, am Deutschen Zentrum für Luft- und Raumfahrt gebaute Hand-Arm System, das vollständig mit variabler Steifigkeitsaktuierung ausgerüstet ist. Da ein Mensch in der Lage ist blind zu prellen, haben wir uns dafür entschieden einen Ballbeobachter, der nur die gemessenen Kontaktkräfte des Handkontakts nutzt, zu benutzen, so dass keine bildverarbeitenden Methoden von Nöten sind.

Contents

1	Introduction	1
2	Modeling	5
2.1	1 DoF Model	5
2.1.1	Free Flight	8
2.1.2	Hand Contact	8
2.1.3	Floor Contact	8
2.1.4	Hand Trajectory	9
2.1.5	Summary	10
2.2	3 DoF Model	10
2.2.1	Ball Model	12
2.2.2	Floor Contact	12
2.2.3	Hand Model	14
2.2.4	Hand Contact	16
2.3	6 DoF Model	17
2.3.1	Ball Model	18
2.3.2	Floor Contact	20
2.3.3	Hand Model	20
2.3.4	Hand Contact	22
2.3.5	Elastic Joint Robot Model	24
3	Control	25
3.1	1 DoF Model	25
3.1.1	Analytic Solution for the Limit Cycle	25
3.1.2	Stability Analysis for Limit Cycle	27
3.1.3	Ball Observer	30
3.1.4	Height Control	34
3.1.5	Summary	36
3.2	3 DoF Model	36
3.2.1	Observer	36
3.2.2	Control	37
3.2.3	Summary	38
3.3	6 DoF Model	38
3.3.1	Observer	38
3.3.2	Control	40
3.3.3	Cartesian impedance control	41
3.3.4	Summary	42

4 Simulations and Experiments	45
4.1 Simulations	45
4.1.1 1 DoF Model	45
4.1.2 3 DoF Model	47
4.1.3 6 DoF Model	47
4.2 Experiments	51
5 Conclusion and Outlook	57
A Newton-Euler Method	59
A.1 Kinematics	59
A.1.1 Translational Kinematics	60
A.1.2 Rotational Kinematics	60
A.2 Dynamics	61
A.2.1 Classification of Forces	61
A.2.2 Newton-Euler Equations	62
A.2.3 D'Alembert's Principle	63
A.2.4 Equations of Motion	64
B Solution for the Hand Contact	65
Bibliography	68

List of Figures

1.1	Dribbling Puma 560.	2
1.2	Highspeed multifingered hand.	2
1.3	Dribbling industrial robot.	3
2.1	Model of the considered 1 DoF dribbling task.	6
2.2	Thermostat as an example of a hybrid system.	7
2.3	Trajectory for the robot hand.	9
2.4	Directed graph of the 1 DoF hybrid dribbling model.	11
2.5	Model of the considered 3 DoF dribbling task.	11
2.6	Free body diagram of the 3 DoF hand contact.	16
2.7	Model of the considered 6 DoF dribbling task.	18
2.8	Elastic dribbling hand.	19
2.9	Rotation order for the robot hand.	21
2.10	Model for the hand contact stiffness K	22
2.11	Reflected stiffness as a function of contact position.	23
3.1	State and notion convention.	26
3.2	Error mapping over one cycle.	28
3.3	Directed graph of the ball observer.	32
3.4	ε and δ regions for observer.	34
3.5	Calculation of the period time.	35
3.6	Block diagram of the 1 DoF model.	36
3.7	Block diagram for the 3 DoF model.	38
3.8	Velocity disturbance observer.	40
3.9	Block diagram for the 6 DoF model.	43
4.1	Positions for the beginning of a 1 DoF simulation.	46
4.2	Energy for the height control of a 1 DoF simulation.	46
4.3	Positions for the beginning of a 3 DoF simulation.	48
4.4	Positions of a sample simulation of the 6 DoF model.	48
4.5	Forces of a sample simulation of the 6 DoF model.	49
4.6	Positions for a reference change in a 6 DoF simulation.	50
4.7	Experimental setup.	51
4.8	Image series of ball initialization.	52
4.9	Image series of a successful dribbling cycle.	53
4.10	Front view series of successful dribbling cycle.	54
4.11	Measured and filtered contact forces.	55
4.12	Observed position of the ball in an experiment.	55

1

Introduction

In this thesis we present the analysis of an elastic dribbling robot for a full spatial motion of the ball. This is an interesting problem in order to further understand how intrinsic elasticity can be used to achieve high-performance and energy efficiency during dynamic and repetitive tasks as e.g. throwing [HWWAS11], walking [YNT98] and batting [OBN02]. We consider the problem of a rather stiff joint torque controlled lightweight arm that is equipped with an intrinsically compliant hand. With this device we intend to sustain a longer ball contact and a more robust control of the ball compared to an intrinsically very stiff robot. The work presented in this thesis intends to lay ground on a future work for full Variable Impedance Actuation (VIA) arms. Recently, a full seven degree of freedom (DoF) VIA arm [GASB⁺11] has been built at the German Aerospace Center (DLR), for which the extension of the methods developed in the present thesis is certainly the next step to take.

Robot dribbling was first introduced in a seminar work in 2001, cf. [Sti] (see Fig. 1.1). The authors used an industrial robot with a half-cylindrical tube for mapping the system to a 2-D system. The control is reactive and pushes the ball downwards if a contact is detected. For the stabilizing of the lateral ball motion they apply a spin to the ball.

[SNI05] utilizes a high-speed multi-fingered hand for dribbling a ping-pong ball (see Fig. 1.2). This experiment served for evaluation of their high-speed vision for ball tracking. They used a hard small plate at the finger tip for dribbling. Besides, they developed a strategy for controlling the ball but did not analyze its stability.

[BSWB09] introduces a basketball playing industrial robot, utilizing a solid plate as hand (see Fig. 1.3). The control relies mainly on the



Figure 1.1: Dribbling Puma 560.

ball tracking vision system and achieves stability of the cycle. They also investigated stability for this model by using a Poincaré map. In experiments they achieved with vision system infinite stable dribbling cycles and without vision system about 20 stable dribbling cycles. In [MSBW10] the authors used an elastic element for prolonging the contact time and storing elastic energy in the system based on an optimal control trajectory. Later in [BMS⁺10] they made experiments with a spring in the hand. In particular, they applied transverse linearization [BH95] for controlling the ball during contact.

Closely related to dribbling is the classical juggling task. [BKK88] investigated this first. the authors used a mirrored and scaled version of the ball trajectory, which means that the ball has to be tracked over the entire cycle. In [RLS07] the first blindly juggling robot was presented. [RD09] used only a linear motor for juggling without the need of active ball tracking, as the lateral motion is stabilized by the shape of the juggling paddle. A stability analysis is given as well.

This thesis provides two main contributions.

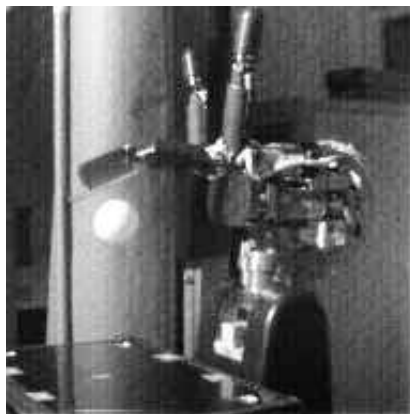


Figure 1.2: Highspeed multifingered hand.



Figure 1.3: Dribbling industrial robot.

The first one is to blindly achieve a stable dribbling cycle with the DLR Lightweight robot III (LWR III). For this, we develop an observer that is capable to estimate the ball state by contact force measurement only. The second question we treat concerns the stabilization of the dribbling task. We present a stability analysis of the vertical ball motion for a sinusoidal hand trajectory together with stabilizing controllers for the lateral ball motion.

The thesis is organized as follows. In Chapter 2 we describe three different models with rising complexity, which are the basis for our analysis and control. The first one describes only a vertical motion and is used for basic analysis of the dribbling task. In the other two models the basketball is able to perform planar and spatial motions. It is used for deriving stabilizing controller actions.

In Chapter 3 we investigate the stability and control of the dribbling task. We present the analytic solution of the model with the vertical motion and a condition for its stability. Furthermore, an observer that can be used for the ball is shown along with a stability analysis for it. Please note that this is achieved although the force measurement is only available during hand contact. For the planar and spatial model we also provide extensions for the observer and a controller for the horizontal translations.

In Chapter 4 we show results obtained from simulations of the pre-mentioned models and from experiments carried out on an LWR III.

Chapter 5 concludes the thesis by recapitulating the achieved results and provides an outlook on future work.

2

Modeling

In this chapter we present the models that were used for investigating basketball dribbling with a robot. Three models with increasing DoF are applied.

- The first model consists only of a vertical DoF. With this we conduct some fundamental stability analysis of the corresponding limit cycle in Chapter 3. Furthermore, we present an observer for the ball position in Sec. 3.1.3. We use this approach to obtain a basic understanding of the ball dribbling process.
- Besides the vertical motion the second model includes also a horizontal and a rotational DoF. Hence, the ball and the robot are able to move freely in a plane. This model is especially used for analyzing the spin of the ball.
- In the third model we remove all constraints from the ball and the robot hand. Hence, in terms of end-effector coordinates they can move in their natural 6 DoF. In this model we also take the dynamics of the robot into account.

2.1 1 DoF Model

In this section we describe the considered model for analyzing the periodic dribbling task in 1 DoF. Furthermore, we introduce the used hand trajectory.

Figure 2.1 depicts a schematic illustration of the considered system. The ball is modeled as a point mass m_B and radius r_B that is able to perform vertical movements denoted by the ball height z_B . The hand

position is denoted by $z(t)$. Furthermore, we consider the hand to be elastic and having zero mass. The associated stiffness K_H is attached to the hand. We use this simplified robot model for studying the essential elements of the vertical elastic dribbling cycles. Furthermore, as the spring is considered to be much more compliant than the robot, we may assume the robot to be a perfect position actuator.

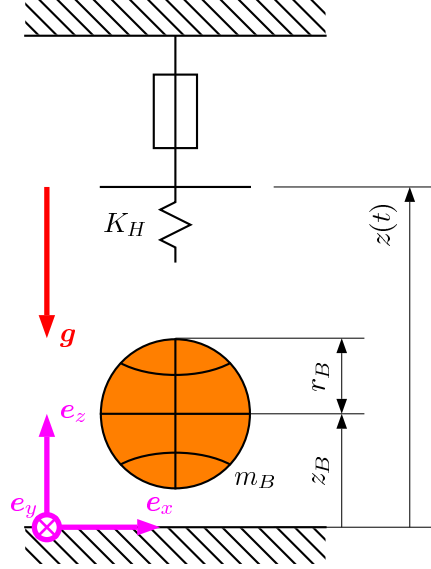


Figure 2.1: Model of the considered 1 DoF dribbling task.

The ball motion is composed of the three phases *free flight*, *hand contact* and *floor contact*. Thus, it is convenient to use a hybrid automaton for modeling, which is defined as follows.

Definition 1 (Hybrid Automaton, cf. [LLL09])

A hybrid automaton H is a tuple

$$H = (\mathcal{Q}, \mathcal{V}, \mathbf{f}, \text{Init}, \text{Inv}, \Theta, \mathcal{G}, \mathcal{R}, \Sigma, \lambda) \quad (2.1)$$

where:

- $\mathcal{Q} = \{q_1, \dots, q_k\}$ is a finite set of discrete states (control locations);
- $\mathcal{V} = \{x_1, \dots, x_n\}$ is a finite set of continuous variables;
- $\mathbf{f} : \mathcal{Q} \times \mathbb{R}^n \rightarrow \mathbb{R}^n$ is an activity function;
- $\text{Init} \subset \mathcal{Q} \times \mathbb{R}^n$ is the set of initial states;
- $\text{Inv} : \mathcal{Q} \rightarrow 2^{\mathbb{R}^n}$ describe the invariants of the locations;
- $\Theta \subseteq \mathcal{Q} \times \mathcal{Q}$ is the transition relation;
- $\mathcal{G} : \Theta \rightarrow 2^{\mathbb{R}^n}$ is the guard condition;

- $\mathcal{R} : \Theta \times 2^{\mathbb{R}^n} \rightarrow 2^{\mathbb{R}^n}$ is the reset map¹;
- Σ is a finite set of synchronization labels;
- $\lambda : \Theta \rightarrow \Sigma$ is the labeling function.

The automaton H describes a set of (hybrid) states $(q, x) \in \mathcal{H} = \mathcal{Q} \times \mathbb{R}^n$.

In Fig. 2.2 we find a thermostat as an example for a hybrid automaton taken from [Lyg] a thermostat. It consists of the two discrete states heating *on* and *off* and one continuous variable x denoting the temperature in [°C]. On the left side the directed graph of the system and on the right side the analytical description of the system are depicted. The heating is switched from *off* to *on* if the temperature falls below 18 °C. The switch from *on* to *off* is activated if the temperature rises above 22 °C. The system can be initialized in every possible state. Those are for the *on* state the temperature less than 22 °C and for the *off* state above 18 °C.

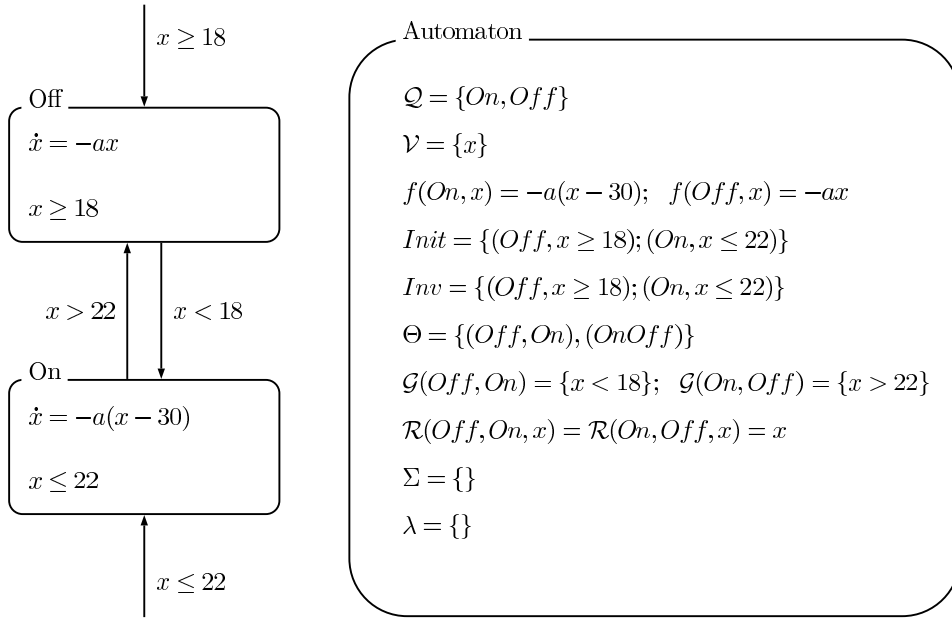


Figure 2.2: Thermostat as an example of a hybrid system.

For the 1 DoF dribbling model we will use two discrete states:

1. free flight (FF),
2. hand contact (HC).

Furthermore, we use in all discrete states the continuous state vector $z_B := [z_{1B} \ z_{2B}]^T = [z_B \ \dot{z}_B]^T$. In the following, we derive the activity

¹At this place there is a small typing error in [LLL09]: $\mathcal{R} : \Theta \rightarrow 2^{\mathbb{R}^n} \times 2^{\mathbb{R}^n}$ is incorrect.

functions and define the remaining part of the hybrid automaton that represents our model.

2.1.1 Free Flight

In the free flight phase there acts only the gravity force on the ball. We obtain the activity function for free flight as

$$\dot{z}_B = \mathbf{f}_1(z_B) = \begin{bmatrix} z_{2B} \\ -g \end{bmatrix}. \quad (2.2)$$

2.1.2 Hand Contact

The hand contact phase is characterized by the linear spring, which anchor point is moving with the desired position $z(t)$ of the hand. Hence, during hand contact z_B is described by the activity function

$$\dot{z}_B = \mathbf{f}_2(z_B, t) = \begin{bmatrix} z_{2B} \\ \frac{K_H}{m_B}(z_{1B} + r_B - z(t)) - g \end{bmatrix}. \quad (2.3)$$

Based on the instantaneous ball position, the hybrid system switches between the free flight and the hand contact state. Finally, if the condition

$$z_{1B} + r_B \geq z(t) \quad (2.4)$$

is fulfilled, the ball is in contact with the hand.

2.1.3 Floor Contact

The floor contact is modeled by a transition in the hybrid system, as the position before and after ground contact remains practically the same, and the velocity changes its sign while losing magnitude. The ground contact is typically in the range of 0.015 s (for a drop height of 1 m), i.e. compared to the overall dribbling cycle negligible [Fon06]. Hence, we introduce a coefficient of restitution (COR) that is defined as

$$COR := -\frac{z_{2B}^+}{z_{2B}^-}, \quad (2.5)$$

with z_{2B}^- being the velocity before and z_{2B}^+ the velocity after contact, see [MMS05]. This instant takes place if the ball reaches the height $z_{1B} = r_B$. The parameter COR is chosen to be 0.85 according to the official rules of basketball [Fé], where the inflation of the ball based on the rebounded height is defined.

2.1.4 Hand Trajectory

In [BKK88] the authors used a mirrored trajectory of the ball for robot juggling, which is essentially a parabola. Furthermore, negative acceleration seems desirable, as it was shown to lead to stable juggling cycles [RD09]. However, instead of a parabola we select a sinusoidal excitation motion of the hand, since during contact the considered system is a second order mass-spring complex. In addition, a positive sine half-wave has also negative acceleration but this changes sign at the end so that the reversal can be carried out faster. This imposes smaller velocity and acceleration requirements on the robot. Lastly, a sine half-wave is also a good approximation for a parabola. In this thesis we compose the hand trajectory from a fast and a slow sine half-wave, which frequency relation is 1 : 4.

The hand trajectory is described by the three parameters amplitude A , offset z_0 , and period time T , respectively the frequency $\omega = 5\pi/(4T)$. Hence, $z(t)$ is

$$z(t) = \begin{cases} A \sin\left(\frac{5\pi}{4T}t\right) + z_0 & \text{for } t \in \left[0; \frac{4}{5}T\right] \\ -\frac{1}{4}A \sin\left(\frac{5\pi}{T}t\right) + z_0 & \text{for } t \in \left]\frac{4}{5}T; T\right[, \end{cases} \quad (2.6)$$

which is two times continuously differentiable. In fig. 2.3 this trajectory is depicted.

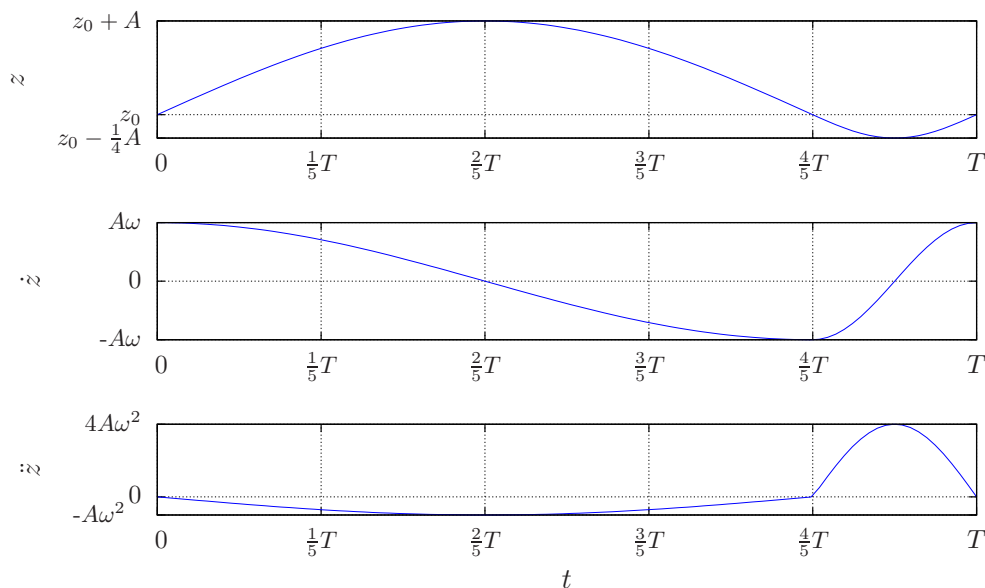


Figure 2.3: Trajectory for the robot hand.

2.1.5 Summary

Summarizing, we can define the remaining elements of the automaton. With the condition for hand contact (2.4) we obtain

$$\mathcal{Q} = \{HC, FF\}, \quad (2.7)$$

$$\mathcal{V} = \{z_{1B}, z_{2B}\}, \quad (2.8)$$

$$f(HC, \mathbf{z}_B) = \mathbf{f}_2(\mathbf{z}_B, t), \quad (2.9)$$

$$f(FF, \mathbf{z}_B) = \mathbf{f}_1(\mathbf{z}_B), \quad (2.10)$$

$$Init = \{(FF, \mathbf{z}_B) | z_{1B} > r_B \wedge z_{1B} < z(0) - r_B\}, \quad (2.11)$$

$$Inv = \{(HC, \mathbf{z}_B \in \mathbb{R}^2 | z_{1B} + r_B \geq z(t)), (FF, \mathbf{z}_B \in (r_B, z(t) - r_B))\}, \quad (2.12)$$

$$\Theta = \{(HC, FF), (FF, HC), (FF, FF)\}, \quad (2.13)$$

$$\mathcal{G}(HC, FF) = \{\mathbf{z}_B \in \mathbb{R}^2 | z_{1B} < z(t) - r_B\}, \quad (2.14)$$

$$\mathcal{G}(FF, HC) = \{\mathbf{z}_B \in \mathbb{R}^2 | z_{1B} \geq z(t) - r_B\}, \quad (2.15)$$

$$\mathcal{G}(FF, FF) = \{\mathbf{z}_B \in \mathbb{R}^2 | z_{1B} < r_B\}, \quad (2.16)$$

$$\mathcal{R}(HC, FF, \mathbf{z}_B) = \mathcal{R}(FF, HC, \mathbf{z}_B) = \mathbf{z}_B, \quad (2.17)$$

$$\mathcal{R}(FF, FF, \mathbf{z}_B) = [z_{1B} - CORz_{2B}]^T, \quad (2.18)$$

$$Init = \{FF, \mathbf{z}_B \in \mathbb{R}^2 | z_{1B} \in (r_B, z(0) - r_B)\}. \quad (2.19)$$

As there are no hybrid automata running in parallel, no synchronization labels and labeling functions are defined.

Overall, the described model can also be represented by the directed graph depicted in Fig. 2.4.

In the following we present models with increasing DoF for the hand and ball.

2.2 3 DoF Model

In the 1 DoF case we used a very simplified model. In the next step we want to extend this to a planar motion. Therefore, we take in addition to the vertical motion spin and a horizontal motion into account. For the 3 DoF model we use the same assumption as in the 1 DoF case: The robot shall be a perfect position actuator.

For the 1 DoF model a very strict model approach was applied in order to study fundamental properties of basketball dribbling. For the remaining higher order models we do not use this strict model approach, as it would not lead to a better insight to the system. Hence, we define a general ball model, which is excited by a force input in the hand and floor contact.

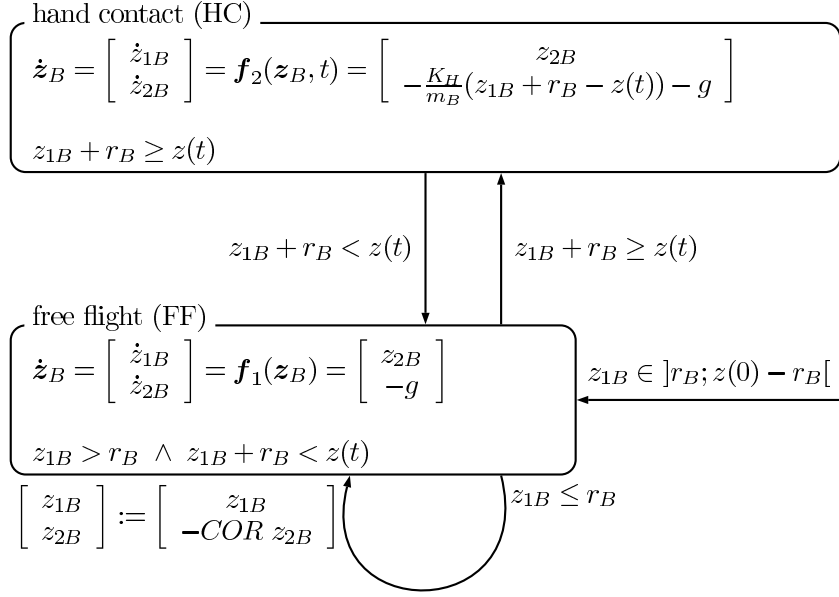


Figure 2.4: Directed graph of the 1 DoF hybrid dribbling model.

The proposed model is depicted in Fig. 2.5. In the upper right corner the robot used for ball dribbling is depicted. Its position is denoted by the 3 DoF $x = [x(t) \ z(t) \ \alpha(t)]^T$. The finger is mounted directly with a rotational bearing and a rotational spring to the robot. It is therefore described by one rotational DoF, denoted by β . Furthermore, it is associated to a mass m_H and an inertia tensor I_H .

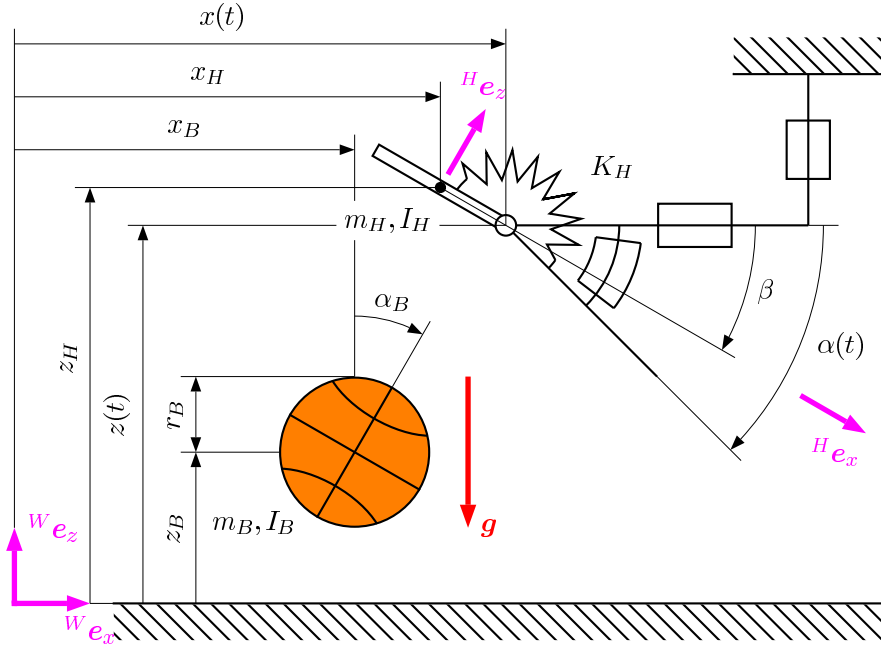


Figure 2.5: Model of the considered 3 DoF dribbling task.

Figure 2.5 shows two relevant frames. One is the world frame $\{W\}$ and the other is the body fixed finger frame $\{H\}$. In the following, nearly all vectors are expressed in $\{W\}$. Hence, we drop the index unless specified otherwise.

In our first experiments we used a hand with three rigid beams and rotational springs as depicted. However, we did not achieve the desired performance with them as the reflected mass of the fingers was simply too high for obtaining significant elastic energy storage or release. Hence, we used in later experiments only the leaf springs and achieved a much better performance. This modeling approach for the spring without mass is presented in Sec. 2.3. However also the mass based finger approach is presented, as the same controller can be used regardless whether the beam is rigid or not.

As the hand contact is quite significant in length we model it continuously. We also use this model for the floor contact. In the following, we first present the ball model with a force input and then the floor contact model. Furthermore, we derive a model for the finger motion and the hand contact force.

2.2.1 Ball Model

In Fig. 2.5 the ball is depicted below the hand and is described by the three coordinates $\mathbf{x}_B = [x_B \ z_B \ \alpha_B]^T$ together with the respective velocities. As the ball is a completely unbounded system there are only forces acting on its perimeter. Apart from gravity g , a force $\mathbf{F}_B = [F_{1B} \ 0 \ F_{3B}]^T$ due to the contact with the hand or the floor is acting directly on the perimeter of the ball. This yields the model equation

$$\begin{bmatrix} \ddot{x}_B \\ \ddot{z}_B \\ \ddot{\alpha}_B \end{bmatrix} = \begin{bmatrix} \frac{F_{1B}}{m_B} \\ \frac{F_{3B}}{m_B} - g \\ \frac{1}{I_B} \mathbf{e}_y(\mathbf{r}_B \times \mathbf{F}_B) \end{bmatrix}, \quad (2.20)$$

with \mathbf{r}_B as the vector from the center of the ball to the point of contact and $\mathbf{e}_y(\mathbf{r}_B \times \mathbf{F}_B)$ as the mapping of the torque vector $\mathbf{r}_B \times \mathbf{F}_B$ to the y axis.

2.2.2 Floor Contact

As we have to define a continuous model for the hand contact that takes the spin of the ball into account, we also use this model for the floor contact instead of the discrete model approach from Sec. 2.1.

The ball is in floor contact if

$$z_B \leq r_B. \quad (2.21)$$

The contact force consists of two components. F_{FC_n} is the normal force and in the floor contact case collinear with the z -axis. F_{FC_t} is the force tangential to the floor plane.

Normal Force

The normal force is calculated by a Hunt-Crossley Model [HC75] that is chosen to be

$$F_{FC_n} = -K_F(z_B - r_B) - D_F(z_B - r_B)\dot{z}_B, \quad (2.22)$$

with K_F being the stiffness and D_F the damping constant.

Tangential Force

The physical effect caused by the tangential force is that due to friction the relative velocity between ball and floor fades away over the contact. This is taken into account by a lumped LuGre model [CT99], which is given as

$$\dot{s} = v_{FC_r} - \frac{\sigma_0 v_{FC_r}}{g(v_{FC_r})} s \quad (2.23)$$

$$F_{FC_t} = (\sigma_0 s + \sigma_1 \dot{s} + \sigma_2 v_{FC_r}) F_{FC_n}, \quad (2.24)$$

with

$$g(v_{FC_r}) = \mu_c + (\mu_s - \mu_c) e^{-|v_{FC_r}/v_s|^\nu}. \quad (2.25)$$

s is the slip between ball and floor, σ_0 the rubber longitudinal lumped stiffness, σ_1 the rubber longitudinal lumped damping, σ_2 the viscous relative damping, μ_c the normalized Coulomb friction, μ_s the normalized static friction, v_s the Stribeck relative velocity, F_n the normal force and v_{FC_r} the relative velocity. The steady-state friction/slip characteristic is captured by ν . The relative velocity for this case is given by

$$v_{FC_r} = \dot{x}_B - r_B \dot{\alpha}_B. \quad (2.26)$$

Therewith, we obtain the force vector of the hand contact by (2.22) and (2.23) as

$$\mathbf{F}_B = \begin{bmatrix} F_{FC_t} \\ 0 \\ F_{FC_n} \end{bmatrix}. \quad (2.27)$$

In addition, the vector from the ball center to the contact point

$$\mathbf{r}_B = \begin{bmatrix} 0 \\ 0 \\ -r_B \end{bmatrix} \quad (2.28)$$

is given. In the following section we present the derivation of the hand model and the hand contact calculation.

2.2.3 Hand Model

For obtaining the equations of motion for the hand we use the Newton-Euler method that is outlined in the appendix A or can be found in [SE04]. We first calculate the kinematics and derive from that the dynamics of the hand. The generalized coordinate is, as mentioned before, β .

Translational Kinematics

According to Fig. 2.5 we can calculate the position vector of the center of mass expressed in the depicted world frame as

$$\mathbf{x}_H = \begin{bmatrix} x(t) - \frac{l_H}{2} \mathbf{c}_\beta \\ 0 \\ z(t) + \frac{l_H}{2} \mathbf{s}_\beta \end{bmatrix}, \quad (2.29)$$

with l_H being the length of the finger. Therefore, we assume that the mass in the finger is uniformly distributed and the cross section is not changing along its length. Furthermore, we consider a rigid body as the spring gains the deformation energy that is introduced by the ball contact. \mathbf{c}_β and \mathbf{s}_β are used as abbreviations for the cosine and sine. With (2.29) we can obtain the velocity by differentiating with respect to time t

$$\mathbf{v}_H = \underbrace{\begin{bmatrix} \frac{l_H}{2} \mathbf{s}_\beta \\ 0 \\ \frac{l_H}{2} \mathbf{c}_\beta \end{bmatrix}}_{=: J_T} \dot{\beta} + \underbrace{\begin{bmatrix} \frac{dx(t)}{dt} \\ 0 \\ \frac{dz(t)}{dt} \end{bmatrix}}_{=: \bar{\mathbf{v}}_H}, \quad (2.30)$$

with the Jacobian of translation J_T and the generalized velocities $\bar{\mathbf{v}}_H$. The accelerations are obtained by a further differentiation

$$\mathbf{a}_H = J_T \ddot{\beta} + \underbrace{\begin{bmatrix} \frac{l_H}{2} \dot{\beta}^2 \mathbf{c}_\beta + \frac{d^2 x(t)}{dt^2} \\ 0 \\ -\frac{l_H}{2} \dot{\beta}^2 \mathbf{s}_\beta + \frac{d^2 z(t)}{dt^2} \end{bmatrix}}_{=: \bar{\mathbf{a}}_H}, \quad (2.31)$$

with the generalized accelerations $\bar{\mathbf{a}}_H$.

Rotational Kinematics

We also define the rotation of the body, which is the rotation from the world frame $\{W\}$ to the body fixed finger frame $\{H\}$. This yields the rotation matrix

$${}^W R_H = \begin{bmatrix} \mathbf{c}_\beta & 0 & \mathbf{s}_\beta \\ 0 & 1 & 0 \\ -\mathbf{s}_\beta & 0 & \mathbf{c}_\beta \end{bmatrix}. \quad (2.32)$$

The rotational velocity is then

$$\boldsymbol{\omega}_H = \underbrace{\begin{bmatrix} 0 \\ 1 \\ 0 \end{bmatrix}}_{=: J_R} \dot{\beta} \quad (2.33)$$

with the Jacobian of rotation J_R . By differentiating (2.33) with respect to time t we obtain the rotational acceleration as

$$\boldsymbol{\alpha}_H = J_R \ddot{\beta}. \quad (2.34)$$

Dynamics

For obtaining the equations of motion we set up the according Newton-Euler equations. For this we define

- the global mass matrix $\overline{\overline{M}} = \text{diag}\{m_H I \ I_H\}$,
- the global Jacobian $\overline{J} = [J_T \ J_R]^T$,
- the global Coriolis force vector $\overline{\boldsymbol{q}}^c = [m_H \overline{\boldsymbol{a}}_H \ \tilde{\boldsymbol{\omega}}_H I_H \boldsymbol{\omega}_H]^T$.

In the global Coriolis force vector the tilde operator of a vector $\boldsymbol{a} = [a_1 \ a_2 \ a_3]^T$ is used, which is defined as

$$\tilde{\boldsymbol{a}} := \begin{bmatrix} 0 & -a_3 & a_2 \\ a_3 & 0 & -a_1 \\ -a_2 & a_1 & 0 \end{bmatrix}. \quad (2.35)$$

This maps the cross product of two vectors $\boldsymbol{a}_1 \times \boldsymbol{a}_2$ to a matrix vector product $\tilde{\boldsymbol{a}}_1 \boldsymbol{a}_2$.

For the global vector of active forces we have to take into account the force due to gravity, the torque applied by the spring and the contact force. The contact force is calculated similarly to the floor contact force in Sec. 2.2.2. We cover this after the derivation of the hand dynamics. Hence, we assume that we know the contact force \boldsymbol{F}_{HC} that is composed of a tangential F_{HC_t} and a normal component F_{HC_n} . These are shown in the free body diagram of the hand contact in Fig. 2.6. The contact position is denoted by δ . For simplicity we assume the finger to be rather thin, so that the forces are directly acting on their center line. The spring depicted in Fig. 2.6 is relaxed for $\alpha = \beta$.

Hence, we obtain the vector of applied forces as

$$\overline{\boldsymbol{q}}^e = \begin{bmatrix} {}^W R_H \begin{bmatrix} F_{HC_t} \\ 0 \\ F_{HC_n} \end{bmatrix} + \begin{bmatrix} 0 \\ 0 \\ -m_H g \end{bmatrix} \\ 0 \\ K_H(\beta - \alpha) + \left(\delta - \frac{l_H}{2}\right) F_{HC_n} \\ 0 \end{bmatrix}. \quad (2.36)$$

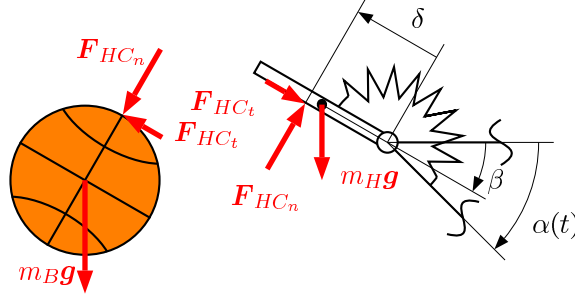


Figure 2.6: Free body diagram of the 3 DoF hand contact.

Therewith, the Newton-Euler Equations is given as

$$\overline{M}\overline{J}\ddot{\beta} + \overline{q}^c = \overline{q}^e + \overline{Q}\overline{q}^r \quad (2.37)$$

with \overline{Q} denoting a distribution matrix and \overline{q}^r denoting the reaction forces. Those can be canceled out by applying D'Alembert's Principle [SE04]. We multiply (2.37) with \overline{J}^T from the left. This yields the equation of motion for the finger.

$$\underbrace{\frac{m_H l_H^2}{3}}_{=:M} \ddot{\beta} + \underbrace{\frac{l_H m_H}{2} \left(\mathbf{s}_\beta \frac{d^2 x(t)}{dt^2} + \mathbf{c}_\beta \frac{d^2 z(t)}{dt^2} \right)}_{=:k} = \underbrace{-\frac{l_H m_H g}{2} \mathbf{c}_\beta + K_H(\alpha(t) - \beta) + \delta F_{HC_n}}_{=:q} \quad (2.38)$$

2.2.4 Hand Contact

For the hand contact we use a similar model as for the floor contact described in Sec. 2.2.2. Since we assume the absence of damping in the normal direction of the hand contact, we set the damping parameter of the Hunt Crossley contact model to zero. This yields

$$F_{HC_n} = K_{HC} ({}^H z_B + r_B). \quad (2.39)$$

Therefore, we use the ball coordinates w.r.t. the finger coordinate system. Hence, the condition for hand contact is

$${}^H z_B \geq -r_B. \quad (2.40)$$

The LuGre model for the tangential force F_{HC_t} is the same as in Sec. 2.2.2. The only difference is the calculation of the relative velocity. The complete relative velocity vector \mathbf{v}_R is obtained from the velocities

\mathbf{v}_{B_p} and \mathbf{v}_{H_p} of the two contacting bodies at the contact point p

$$\begin{aligned} \mathbf{v}_R = \mathbf{v}_{H_p} - \mathbf{v}_{B_p} &= (\mathbf{v}_H + \boldsymbol{\omega}_H \times \mathbf{r}_{H,C}) - (\mathbf{v}_B + \boldsymbol{\omega}_B \times \mathbf{r}_B) \\ &= \begin{bmatrix} \delta \mathbf{s}_\beta + \frac{dx}{dt} \\ 0 \\ \delta \mathbf{s}_\beta + \frac{dz}{dt} \end{bmatrix} \\ &\quad - \left(\begin{bmatrix} \dot{x}_B \\ 0 \\ \dot{z}_B \end{bmatrix} + \begin{bmatrix} 0 \\ \dot{\alpha}_B \\ 0 \end{bmatrix} \times \left({}^W R_H \begin{bmatrix} 0 \\ 0 \\ r_B \end{bmatrix} \right) \right), \end{aligned} \quad (2.41)$$

with $\mathbf{r}_{H,C}$ being the position vector from the center of mass of the finger to the contact point, \mathbf{v}_B and $\boldsymbol{\omega}_B$ being the translational and rotational ball velocity and ${}^H \mathbf{r}_B = [0 \ 0 \ r_B]^T$ being the vector from the ball center to the contact point. The desired tangential relative velocity is obtained by mapping \mathbf{v}_R to the x -axis of the $\{H\}$ frame, which is

$$\mathbf{v}_{R_t} = \mathbf{v}_R {}^H e_x. \quad (2.42)$$

The normal direction can be fed directly into the equation of motion for the finger, as there is no vectorial quantity needed. Furthermore, as the tangential force is acting directly on the bearing of the finger, it is not needed in the finger model.

For the ball model we use the unit vectors of the $\{H\}$ frame as the direction of the tangential and normal forces. This yields

$$\mathbf{F}_B = {}^W R_H \begin{bmatrix} F_{HC_t} \\ 0 \\ F_{HC_n} \end{bmatrix} \quad (2.43)$$

as the force vector that is acting on the ball.

2.3 6 DoF Model

In this section we outline the ball and hand model suitable for 6-DoF dribbling task. The dynamic model for the robot is taken as granted. The Cartesian impedance control will be introduced in Sec. 3.3.3. Therefore, we first consider the end effector of the robot only and assume it as a virtual driving input for position, rotation and velocity. A schematic view of the model is depicted in Fig. 2.7. In reality we use three fingers that are mounted along one common plane, cf. Fig. 2.8. The fingers are made of spring steel, while for impact damping issues thin foam is glued onto them.

In the modeling part, we assume the fingers to be massless and use only their respective spring characteristics, cf. Fig. 2.7. Both bodies are described by their respective position and orientation. The relevant frames are the effector frame $\{EE\}$, the world frame $\{W\}$ (located on

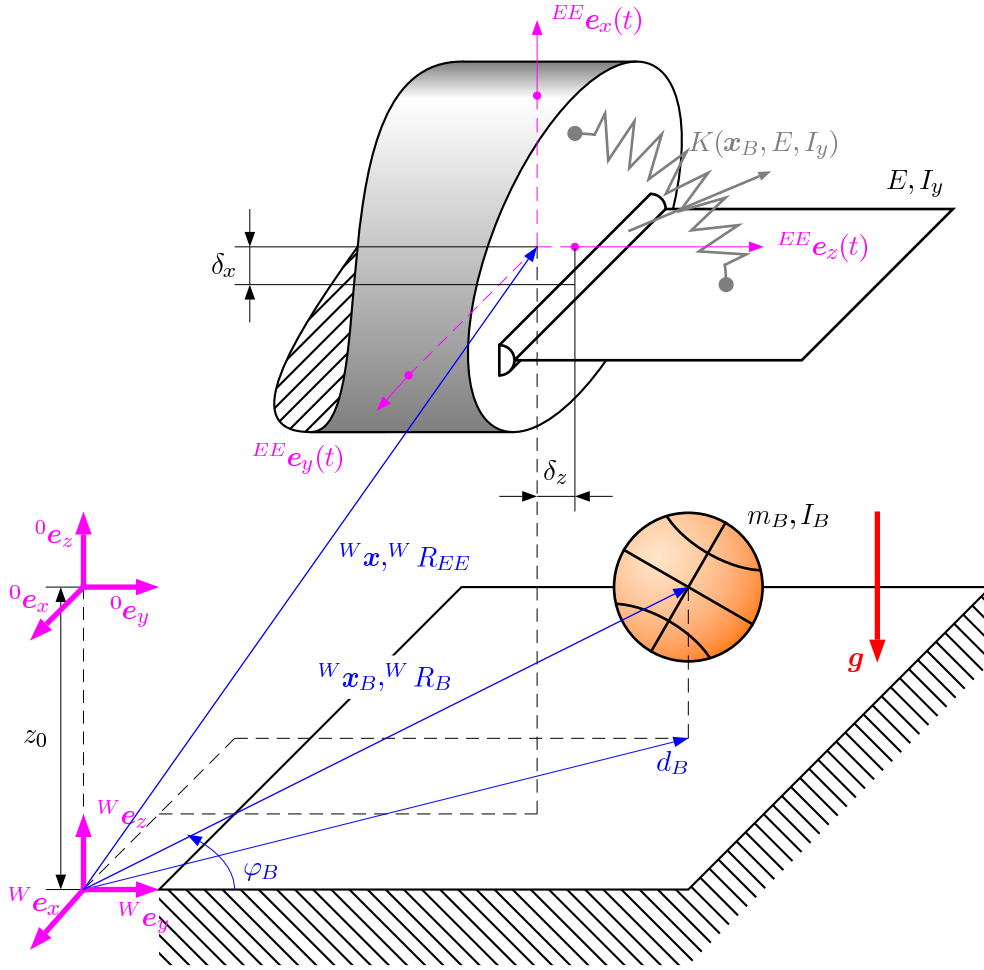


Figure 2.7: Model of the considered 6 DoF dribbling task.

the floor), and the base frame $\{0\}$ (above the world frame). The spring mounting is translated into the $\{EE\}$ frame by the offsets δ_z and δ_x .

In the following, we derive a suitable ball model and then show how to obtain the relevant forces acting on the ball. All vectors will be expressed in $\{W\}$ unless specified otherwise. Hence, we drop the index for the frame.

2.3.1 Ball Model

The ball is modeled as a free body with the gravity vector g and the force F_B acting on its perimeter. Therefore, it is described by three translational coordinates $x_B = [x_B \ y_B \ z_B]^T$, the respective velocity \dot{x}_B , the quaternion $\xi_B = [q_0 \ q_1 \ q_2 \ q_3]^T$, and three rotational velocities $\omega_B =$

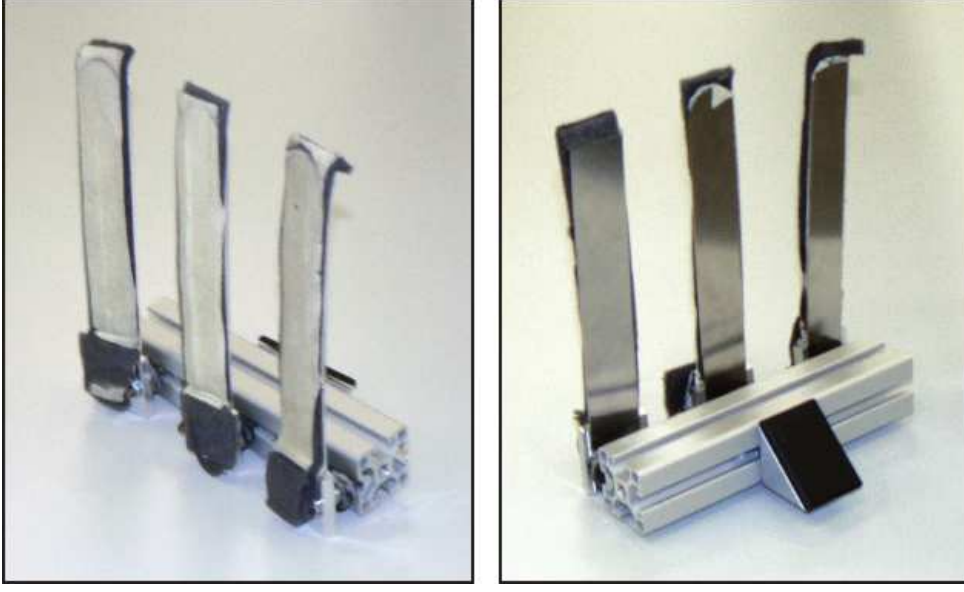


Figure 2.8: Elastic dribbling hand used for the experiments with the DLR Lightweight-Robot III.

$[\alpha_B \ \beta_B \ \gamma_B]^T$ about the axes of $\{W\}$. This yields

$$\begin{bmatrix} \ddot{x}_B \\ \dot{\xi}_B \\ \dot{\omega}_B \end{bmatrix} = \begin{bmatrix} \frac{1}{m_B} \mathbf{F}_B + \mathbf{g} \\ \frac{1}{2} Q(\xi_B) \omega_B \\ I_B^{-1} (\mathbf{r}_B \times \mathbf{F}_B) \end{bmatrix}, \quad (2.44)$$

with \mathbf{r}_B being the vector from the ball center to the force application point, and I_B denoting the ball inertia tensor, which is diagonal due to the ball's rotational symmetry. As we assume the ball to be a spherical shell we obtain [GF04]

$$I_B = \begin{bmatrix} \frac{2}{3} m_B r_B & 0 & 0 \\ 0 & \frac{2}{3} m_B r_B & 0 \\ 0 & 0 & \frac{2}{3} m_B r_B \end{bmatrix}. \quad (2.45)$$

$Q(\xi_B)$ is a matrix that maps Cartesian velocities ω_B to quaternion velocities [SE04]

$$Q(\xi_B) = \begin{bmatrix} -q_1 & -q_2 & -q_3 \\ q_0 & q_3 & -q_2 \\ -q_3 & q_0 & q_1 \\ q_2 & -q_1 & q_0 \end{bmatrix}. \quad (2.46)$$

The calculation of the force \mathbf{F}_B for the different phases is derived in the following paragraphs.

For the control presented later it is useful to have the translational coordinates also in cylindrical coordinates $\mathbf{x}_{B_c} = [\varphi_B \ d_B \ z_B]^T$, see Fig. 2.7. These are obtained via

$$\mathbf{x}_{B_c} = \begin{bmatrix} \varphi_B \\ d_B \\ z_B \end{bmatrix} = \begin{bmatrix} \arctan 2(-x_B, y_B) \\ \sqrt{x_B^2 + y_B^2} \\ z_B \end{bmatrix}, \quad (2.47)$$

with $\arctan 2(-x_B, y_B)$ as the arctangent function that takes all quadrants into account.

2.3.2 Floor Contact

For the floor contact in the 6 DoF model we can use the same LuGre model as the one for the 3 DoF model in Sec. 3.2.2. The normal force points again in the z direction. For the tangential force we have to calculate the relative velocity between ball and floor. This yields

$$\mathbf{v}_{FC_r} = [\mathbf{0} \ e_y \ e_z] \dot{\mathbf{x}}_B + \begin{bmatrix} 0 \\ 0 \\ -r_B \end{bmatrix} \times \boldsymbol{\omega}_B. \quad (2.48)$$

(2.48) provides also the direction of the tangential force, as it acts in opposite direction to the relative velocity direction. The vector from the ball center to the contact point is the same as in the 2 DoF model, cf. (2.28).

2.3.3 Hand Model

The robot end-effector will later be commanded via a desired frame (actually position and unit quaternion) in Cartesian impedance control (see Sec. 3.3.3). The rotation matrix is described by a well chosen set of Euler angles, whose rotation order is depicted in Fig. 2.9.

The first coordinate system $\{C\}$ is collinear to the base frame. The first rotation acts around the y -axis and is later used for controlling the ball along the d_B coordinate. It is obtained as

$${}^C R_{e_y}(\beta) = \begin{bmatrix} c_\beta & 0 & s_\beta \\ 0 & 1 & 0 \\ -s_\beta & 0 & c_\beta \end{bmatrix}. \quad (2.49)$$

Thereafter, the coordinate system is rotated around the new z -axis, which will be used for controlling the ball along the φ_B coordinate. This yields

$${}^{C'} R_{e'_z}(\gamma) = \begin{bmatrix} c_\gamma & -s_\gamma & 0 \\ s_\gamma & c_\gamma & 0 \\ 0 & 0 & 1 \end{bmatrix}. \quad (2.50)$$

The last rotation is around the z -axis of the base frame and is used for tracking the ball position. To obtain this rotation matrix we first calculate the unit vector e_z expressed in the $\{C''\}$ coordinate system, which is

$${}^{C''} e_z = {}^{C''} R_C {}^C e_z = \left({}^C R_{e_y}(\beta) {}^{C'} R_{e'_z}(\gamma) \right)^T {}^C e_z = \begin{bmatrix} -s_\beta c_\gamma \\ s_\beta s_\gamma \\ c_\beta \end{bmatrix}. \quad (2.51)$$

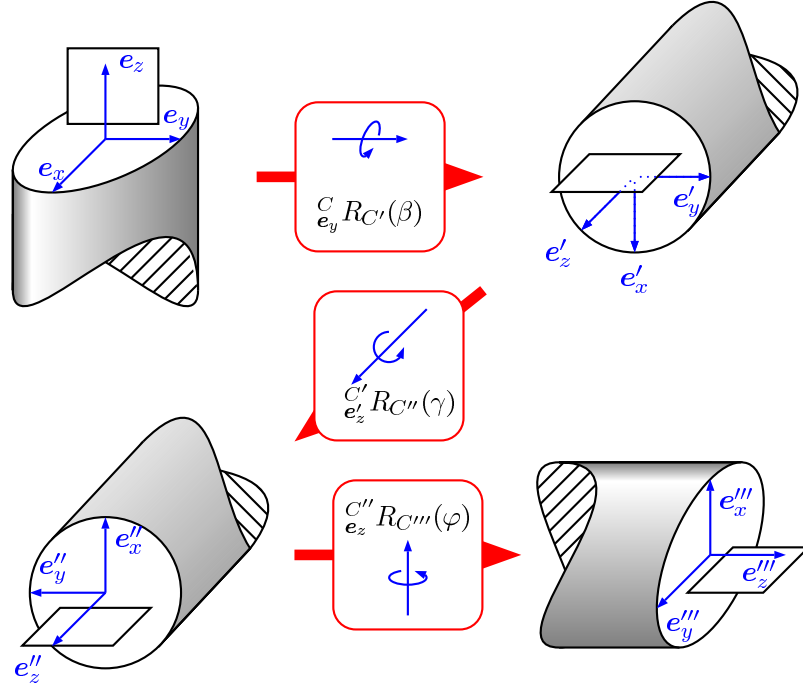


Figure 2.9: Rotation order for commanding the orientation of the robot hand.

The rotation matrix is then obtained from, cf. [SE04],

$${}^{C'''}_{e_z} R_{C'''}(\varphi) = I + {}^{C''} \tilde{e}_z \mathbf{s}_\varphi + {}^{C''} \tilde{e}_z {}^{C''} \tilde{e}_z (1 - c_\varphi c) \quad (2.52)$$

with the tilde operator defined according to (2.35). Hence, we get the overall rotation matrix as

$$\begin{aligned} {}^{C'''}_{e_z} R_C &= {}^C_{e_y} R_{C'}(\beta) {}^{C'}_{e_z} R_{C''}(\gamma) {}^{C''}{}_{e_z} R_{C'''}(\varphi) \\ &= \begin{bmatrix} -\mathbf{s}_\varphi \mathbf{s}_\gamma - \mathbf{c}_\beta \mathbf{c}_\gamma \mathbf{c}_\varphi & -\mathbf{c}_\gamma \mathbf{s}_\varphi - \mathbf{c}_\beta \mathbf{s}_\gamma \mathbf{c}_\varphi & \mathbf{s}_\beta \mathbf{c}_\varphi \\ \mathbf{c}_\varphi \mathbf{s}_\gamma + \mathbf{c}_\beta \mathbf{c}_\gamma \mathbf{s}_\varphi & \mathbf{c}_\gamma \mathbf{c}_\varphi - \mathbf{s}_\beta \mathbf{s}_\gamma \mathbf{s}_\varphi & \mathbf{s}_\beta \mathbf{s}_\varphi \\ -\mathbf{s}_\beta \mathbf{c}_\gamma & \mathbf{s}_\beta \mathbf{s}_\gamma & \mathbf{c}_\beta \end{bmatrix}. \end{aligned} \quad (2.53)$$

We can also calculate the rotational velocity vector, cf. [SE04]

$$\tilde{\omega} = \dot{R} R^T. \quad (2.54)$$

This yields

$$\omega = \begin{bmatrix} \dot{\gamma} \mathbf{s}_\beta \mathbf{c}_\varphi - \dot{\beta} \mathbf{s}_\varphi \\ \dot{\gamma} \mathbf{s}_\beta \mathbf{s}_\varphi + \dot{\beta} \mathbf{c}_\varphi \\ \dot{\varphi} + \dot{\gamma} \mathbf{c}_\beta \end{bmatrix}. \quad (2.55)$$

2.3.4 Hand Contact

The hand contact is calculated similarly to the floor contact. Therefore, it is advantageous to use the position vector of the ball expressed in $\{EE\}$. The condition for hand contact is

$${}^{EE}x_B \geq \delta_x - r_B. \quad (2.56)$$

We assume that there is no damping present in the hand, as the fingers are made of spring steel. Hence, we get

$${}^{EE}F_{HC_n} = -K(\mathbf{x}_B, E, I_y)(+{}^{EE}x_B - \delta_x + r_B) \quad (2.57)$$

for the normal direction of the contact. The stiffness $K(\mathbf{x}_B, E, I)$ is calculated from the linear theory on Bernoulli beams, see Fig. 2.10. The beam is firmly clamped on the left side with the two reactions M_R and N . F denotes the force that is applied by the ball. This causes the bending line $w(z)$, which is calculated by [MMS05]

$$EI_y \frac{d^2 w(z)}{dz^2} = -M_y(z). \quad (2.58)$$

E is the modulus of elasticity, I_y is the geometrical moment of inertia around the y -axis, and M_y is the bending moment around y , which is obtained as

$$M_y(z) = \underbrace{Fz_F}_{=M_R} - \underbrace{Fz}_{=N} + \begin{cases} 0 & \text{for } z \leq z_F \\ F(z - z_F) & \text{for } z > z_F \end{cases}. \quad (2.59)$$

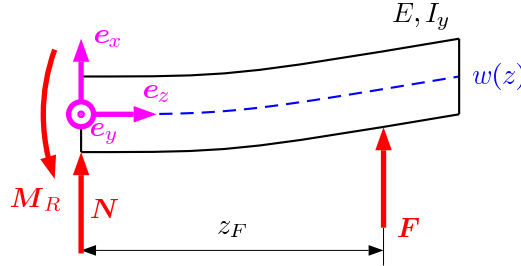


Figure 2.10: Calculation of spring stiffness K seen at the contact point.

By evaluating (2.58) at z_F we obtain a relation between the force and the bending at z_F as

$$F = \underbrace{\frac{EI_y}{3z_F^3}}_{=:K} w(z_F). \quad (2.60)$$

Therewith, the stiffness K seen at the contact point is known. In Fig. 2.11 the stiffness over the length of the hand is depicted. As the stiffness decreases by $1/z^3$ for increasing z we have a high stiffness for small distances.

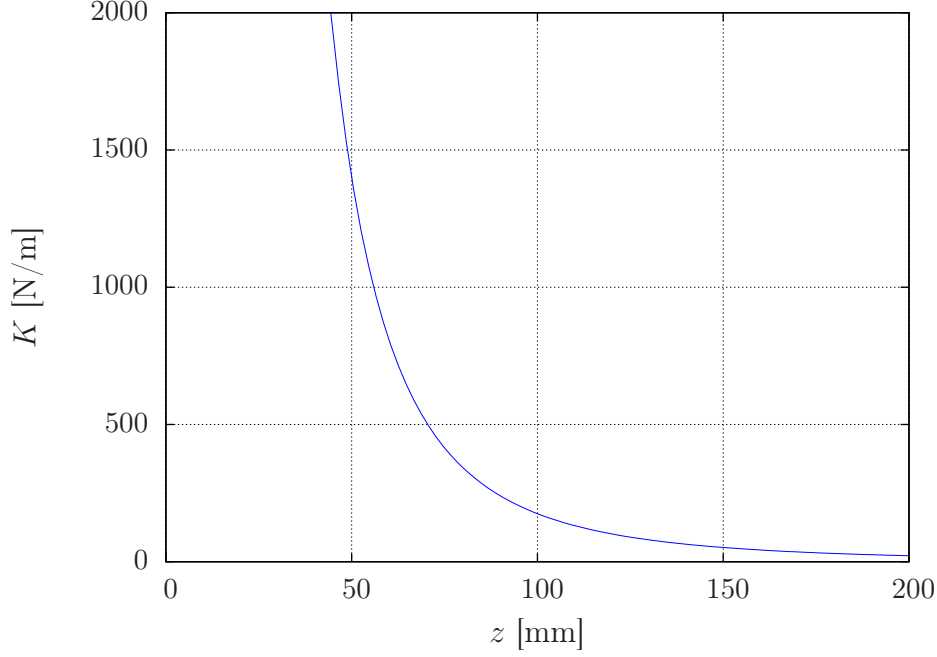


Figure 2.11: Reflected stiffness as a function of contact position.

The tangential direction of the force \mathbf{F}_{HC_t} is calculated analogously to Sec. 2.3.2 by utilizing a LuGre model. The required relative velocity is

$$\begin{aligned} \mathbf{v}_R = \mathbf{v}_P - \mathbf{v}_{B_p} = & (\dot{\mathbf{x}} + \boldsymbol{\omega} \times \mathbf{r}_{EE,C}) - (\dot{\mathbf{x}}_B + \boldsymbol{\omega}_B \times \mathbf{r}_B) \\ & \left(\dot{\mathbf{x}} + \boldsymbol{\omega} \times \left({}^W R_{EE} \left({}^{EE} \mathbf{x}_B + \begin{bmatrix} r_B \\ 0 \\ 0 \end{bmatrix} \right) \right) \right) \\ & - \left(\dot{\mathbf{x}}_B + \boldsymbol{\omega}_B \times \left({}^W R_{EE} \begin{bmatrix} r_B \\ 0 \\ 0 \end{bmatrix} \right) \right) \end{aligned} \quad (2.61)$$

with $\mathbf{r}_{EE,C}$ as the position vector from EE to the contact (see below (2.65)) and ${}^{EE} \mathbf{r}_B := [r_B \ 0 \ 0]^T$ as the vector from the ball center to the point of contact. The tangential relative velocity is obtained by mapping \mathbf{v}_R to the plane of the fingers which is described by the y and z direction of the $\{EE\}$ frame. This yields

$${}^{EE} \mathbf{v}_{R_T} = \begin{bmatrix} 0 & 0 & 0 \\ 0 & 1 & 0 \\ 0 & 0 & 1 \end{bmatrix} {}^{EE} R_W \mathbf{v}_R. \quad (2.62)$$

For the LuGre model we use the norm of the tangential relative velocity. This yields the complete contact force

$$\mathbf{F}_B = {}^W R_{EE} \begin{bmatrix} F_{HC_n} \\ 0 \\ 0 \end{bmatrix} - \frac{\mathbf{v}_{R_T}}{|\mathbf{v}_{R_T}|} F_{HC_T}. \quad (2.63)$$

This contact force is also applied to the robot as an external contact wrench by moving the wrench $\mathcal{F}_{HC} = [\mathbf{F}_B^T \ \mathbf{0}]^T$ into the $\{EE\}$ frame by

$$\mathcal{F}_{ext} = \begin{bmatrix} I & 0 \\ -\tilde{\mathbf{r}}_{C,EE} & I \end{bmatrix} \mathcal{F}_{HC}, \quad (2.64)$$

with $\tilde{\mathbf{r}}_{C,EE}$ being the matrix obtained from applying the tilde operator from (2.35) to the position vector from the contact point to the origin of EE which is

$$\mathbf{r}_{C,EE} = -\mathbf{r}_{EE,C} = -{}^W R_{EE} ({}^{EE} \mathbf{x}_B + {}^{EE} \mathbf{r}_B). \quad (2.65)$$

For the 6 DoF model we want to take the full dynamic model and control of a Cartesian impedance controlled robot into consideration. Therefore, we introduce the underlying set of equations describing the robot dynamics next. The controller is outlined in Sec. 3.3.3.

2.3.5 Elastic Joint Robot Model

Due to the lightweight design of the LWR-III it is not sufficient to model the robot by a second-order rigid body model. The non negligible joint elasticity between motor and link inertia caused by the Harmonic Drive gears and the joint torque sensor has to be taken into account into the model equation. For such a robot the following flexible joint model can be assumed [Spo87]:

$$M(\mathbf{q})\ddot{\mathbf{q}} + C(\mathbf{q}, \dot{\mathbf{q}})\dot{\mathbf{q}} + \mathbf{g}(\mathbf{q}) = \boldsymbol{\tau}_a + \boldsymbol{\tau}_{ext} \quad (2.66)$$

$$B\ddot{\boldsymbol{\theta}} + \boldsymbol{\tau}_a = \boldsymbol{\tau}_m - \boldsymbol{\tau}_f \quad (2.67)$$

$$\boldsymbol{\tau}_a = \boldsymbol{\tau} + DK^{-1}\dot{\boldsymbol{\tau}} \quad (2.68)$$

$$\boldsymbol{\tau} = K(\boldsymbol{\theta} - \mathbf{q}) \quad (2.69)$$

with \mathbf{q} being the link side position, $\boldsymbol{\theta}$ the motor position, $\boldsymbol{\tau}$ the elastic joint torque, $\boldsymbol{\tau}_f$ the friction torque in the motor, $\boldsymbol{\tau}_m$ the motor torque, $M(\mathbf{q})$ the mass matrix, $C(\mathbf{q}, \dot{\mathbf{q}})$ the centripetal and Coriolis vector, $\mathbf{g}(\mathbf{q})$ the gravity vector, $K = \text{diag}\{K_i\}$ the diagonal positive definite joint stiffness matrix, and $B = \text{diag}\{B_i\}$ the diagonal positive definite motor inertia matrix.

The external joint torque is generated by the ball contact wrench measured in the wrist sensor via $\boldsymbol{\tau}_{ext} = J^{TEE} \mathcal{F}_{ext}$, with J being the $\{EE\}$ Jacobian of the manipulator.

3

Control

In the preceding chapter we introduced the models that are used for the analysis and control of robotic dribbling in this chapter. Analogue to Chapter 2 we first analyze the 1 DoF dribbling. Thereafter, we present the extension of the observer and control schemes from the 1 DoF model to the 3 DoF model. With a further extension the control and observer for the whole 6 DoF model is given. Finally, we shortly summarize the Cartesian impedance control that is used for controlling the robot.

3.1 1 DoF Model

In this section we present some fundamental investigations on the stability of a dribbling limit cycle. First, we give a condition if an initial condition for the ball $z_B(0)$ in conjunction with a hand trajectory defined by its amplitude A , height z_0 and period time T yields a stable cycle. Furthermore, we present the analysis of the limit cycle stability. As we only use proprioceptive information, we need an observer for being able to track the ball on the dribbling cycle. For this we derive a suitable observer structure and give a proof for its convergence and stability.

3.1.1 Analytic Solution for the Limit Cycle

Figure 3.1 depicts the time instants at which the hybrid system changes its state node. State vectors at these time instants are denoted with a Roman number and are depicted at the top of the figure.

The states between these time instants are indicated red in the figure.

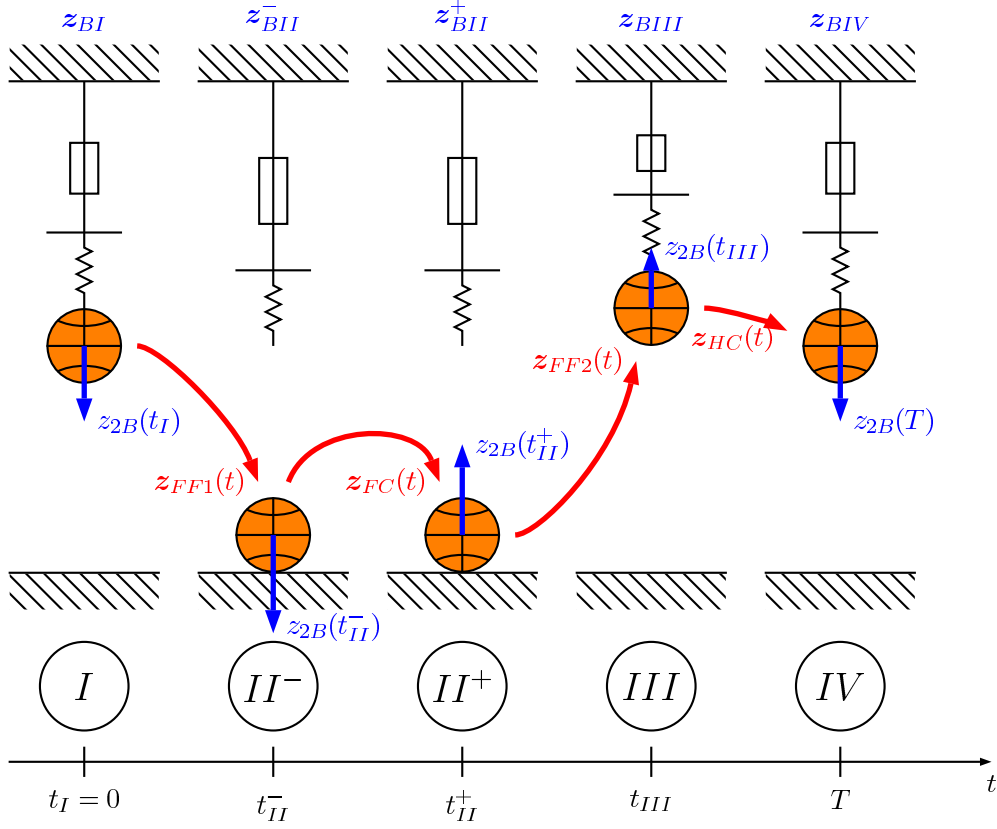


Figure 3.1: State and notion convention.

At $t_I = 0$ s the hand contact is over and the initial ball state is $z_{BI} := z_B(0) = [z_{1BI} \ z_{2BI}]^T$. The velocity is defined to be negative so that the first phase of the ball is free flight. This is described by $z_{FF1}(t)$. t_{II}^- denotes the time instant at which the ball impacts the floor. The ball state at this time instant is z_{BII}^- . As the floor contact is assumed to be a transition in the directed graph of Fig. 2.4 we use $t_{II}^+ = t_{II}^-$ as the time instant after floor contact and z_{BII}^+ as the ball state. The next relevant time instant is t_{III} that denotes the beginning of the hand contact with the corresponding ball state z_{BIII} . The last interesting time instant is the end of the period, denoted by $t_{IV} = T$ and the ball state z_{BIV} .

For the free flight phase we simply get

$$z_{FF1}(t) = \begin{bmatrix} -\frac{1}{2}gt^2 + z_{2BI}t + z_{1BI} \\ -gt + z_{2BI} \end{bmatrix}. \quad (3.1)$$

The time instant t_{II}^- at which the ground contact occurs can be obtained by intersection of $z_{1FF1}(t)$ with the straight $z = r_B$. We label this as the state $z_{BII}^- = z_B(t_{II}^-)$. The floor contact is then characterized by

$$z_{BII}^+ = \begin{bmatrix} z_{1BII}^- \\ -COR \ z_{2BII}^- \end{bmatrix} \quad (3.2)$$

and the solution for the second free-flight phase is

$$z_{FF2}(t) = \begin{bmatrix} -\frac{1}{2}g(t - t_{II}^+)^2 + z_{2BII}^+(t - t_{II}^+) + z_{1BII}^+ \\ -g(t - t_{II}^+) + z_{2BII}^+ \end{bmatrix}. \quad (3.3)$$

The next time instant that has to be calculated is the start of the hand contact. As this corresponds to the intersection of a sine with a parabola, no analytic solution can be provided. Therefore, we approximate the sine of the hand motion by a parabola

$$z_{appr}(t) = a + b \left(t - \frac{\pi}{2\omega} \right)^2 \approx z(t), \quad (3.4)$$

where the parameters a, b are selected such that they minimize the error criterion

$$J = \int_0^{\frac{\pi}{\omega}} (z_{appr} - z(t)) dt, \quad (3.5)$$

which yields

$$\begin{bmatrix} a \\ b \end{bmatrix} = \begin{bmatrix} \frac{1}{\pi^3} (-3A\pi^2 + 60A + z_0\pi^3) \\ \frac{1}{\pi^5} (60\omega^2 A(\pi^2 - 12)) \end{bmatrix}. \quad (3.6)$$

In addition, the cycle begins and consequently ends with the separation of the hand contact. Hence, the hand trajectory needs to be shifted along the time axis such that $z(T) = z_{1BI} + r_B$, which can be found as

$$t := t + \omega T - \underbrace{\frac{\arcsin\left(\frac{r_B - z_0 + z_{1I}}{A}\right)}{\omega}}_{t_{off}}. \quad (3.7)$$

With (3.4) both, the time t_{III} and the state $z_{BIII} := z_{FF2}(t_{III})$ are calculated. Therewith, it is possible to obtain the analytic solution for the hand contact, cf. appendix B,

$$z_{HC}(t) = \Phi \begin{bmatrix} \sin\left(\sqrt{\frac{K_H}{m_B}}(t - t_{III})\right) \\ \cos\left(\sqrt{\frac{K_H}{m_B}}(t - t_{III})\right) \\ \sin(\omega(t - t_{III})) \\ \cos(\omega(t - t_{III})) \end{bmatrix}, \quad (3.8)$$

with Φ being a $[2 \times 4]$ matrix depending on z_{BIII} , the parameters of the hand trajectory, m_B , and K_H . With the relation $z_{HC}(T) \stackrel{!}{=} z_{BI}$ we may inspect whether the chosen parameters result in a valid cycle.

In the next section we analyze the stability of the open loop system.

3.1.2 Stability Analysis for Limit Cycle

For investigating the stability properties of the system, we use a similar method to the one described in [RD09]. For the analysis we suppose that we have found parameters for a closed cycle according to the model shown in Sec. 2.1.

By perturbing the initial conditions of the cycle we elaborate a mapping of the error at the cycle start to its end. For this, we use an iterative method, which is summarized in Fig. 3.2. The overall error mapping ${}^{IV}M_I$ is constructed from the concatenation of the partial mappings iM_j .

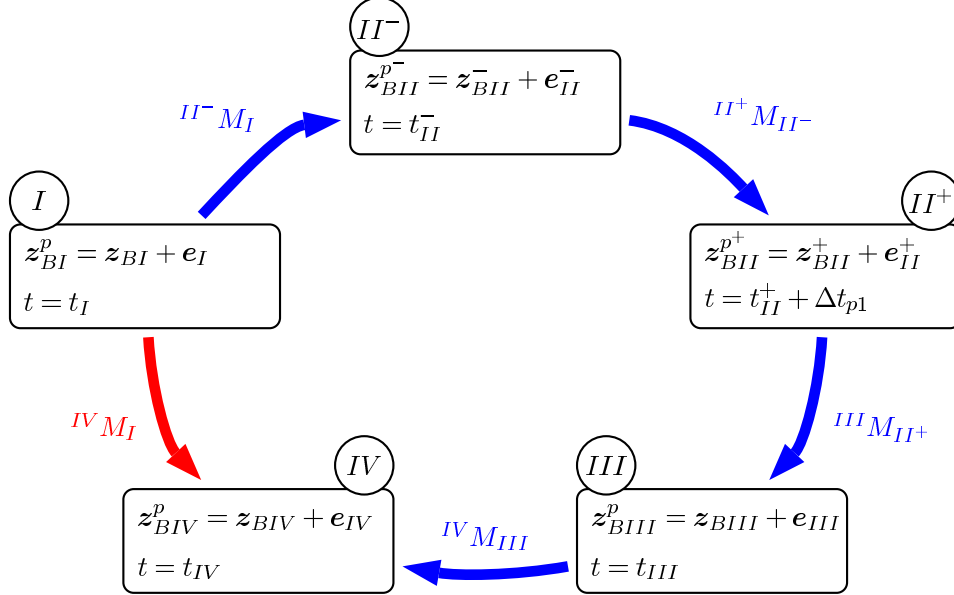


Figure 3.2: Error mapping over one cycle.

Free flight

For free flight we define a new perturbed initial condition

$$z_{BI}^p = z_{BI} + e_I, \quad (3.9)$$

where $e_I = [e_{1I} \ e_{2I}]^T$ is the initial perturbation. Using the new initial condition (3.9) for the free flight we get a perturbed state z_{BII}^{p-} at the nominal floor contact time t_2^- . As we assume to have small errors, we may take the linearization around the nominal unperturbed solution

$$\begin{aligned} z_{BII}^{p-} &= \underbrace{z_{BII}^{p-} \Big|_{e_I=0}}_{z_{BII}^-} + \underbrace{\frac{\partial z_{BII}^{p-}}{\partial e_I} \Big|_{e_I=0}}_{=: {}^{II-}M_I} e_I \\ &= z_{BII}^- + e_{II}^-. \end{aligned} \quad (3.10)$$

The matrix ${}^{II-}M_I$ thereby maps the error e_I at t_1 to the error e_{II}^- at t_2^- and is found to be

$${}^{II-}M_I = \begin{bmatrix} 1 & t_2^- \\ 0 & 1 \end{bmatrix}. \quad (3.11)$$

Floor contact

Since the nominal contact time is not the real one anymore, we have to calculate the perturbed contact time. Therefore, we take the perturbed free flight trajectory from the initial value defined in (3.10), which is obtained as

$$\mathbf{z}_{FF1}^p = \begin{bmatrix} -\frac{1}{2}gt^2 + z_{2BII}^{p-}t + z_{1BII}^{p-} \\ gt + z_{2BII}^{p-} \end{bmatrix} \quad (3.12)$$

and calculate a new intersection time Δt_{p1} . With the trajectory of error defined after nominal floor contact

$$\mathbf{e}_{FC}(t) = \mathbf{z}_{FF2}(t - t_{II}^-) - \mathbf{z}_{FF1}^p(t) \quad (3.13)$$

we are able to calculate the error at this time instant. Therefore, we have to consider that the perturbed trajectory is also performing a floor contact, which yields

$$\mathbf{e}_{FC}(\Delta t_{p1}) = \mathbf{z}_{FF2}(\Delta t_{p1} - t_{II}^-) - \begin{bmatrix} -\frac{1}{2}g\Delta t_{p1}^2 + z_{2BII}^{p-}\Delta t_{p1} + z_{1BII}^{p-} \\ g\Delta t_{p1} + z_{2BII}^{p-} \end{bmatrix}. \quad (3.14)$$

We obtain for the linearization of $\mathbf{e}_{FC}(\Delta t_{p1})$ at $\mathbf{e}_{II}^- = \mathbf{0}$

$$\mathbf{e}_{FC}^{lin}(\Delta t_{p1}) = \underbrace{\mathbf{e}_{FC}(\Delta t_{p1})|_{\mathbf{e}_{II}^- = \mathbf{0}}}_{=0} + \underbrace{\frac{\partial \mathbf{e}_{FC}(\Delta t_{p1})}{\partial \mathbf{e}_{II}^-}}_{=: {}^{II+}M_{II-}} \Big|_{\mathbf{e}_{II}^- = \mathbf{0}} \mathbf{e}_{II}^- \quad (3.15)$$

with the error mapping matrix

$${}^{II+}M_{II-} = \begin{bmatrix} COR & 0 \\ \frac{g(COR+1)}{z_{2BII}} & COR \end{bmatrix}. \quad (3.16)$$

Free flight

The second free flight phase is calculated from the time instant of the perturbed floor contact $t_2^- + \Delta t_{p1}$. We take a new initial condition for the free flight as

$$\mathbf{z}_{BII}^{p+} = \mathbf{z}_{FF2}(t_2^- + \Delta t_{p1}) + \mathbf{e}_{II}^+. \quad (3.17)$$

In the second free flight phase we obtain the same mapping as for the first free flight phase. This yields

$$\begin{aligned} \mathbf{z}_{BIII}^p &= \underbrace{\mathbf{z}_{BIII}^p|_{\mathbf{e}_{BII}^+ = \mathbf{0}}}_{\mathbf{z}_{BIII}} + \underbrace{\frac{\partial \mathbf{z}_{BIII}^p}{\partial \mathbf{e}_{BII}^+}}_{=: {}^{III}M_{II+}} \Big|_{\mathbf{e}_{BII}^+ = \mathbf{0}} \mathbf{e}_{II}^+ \\ &= \mathbf{z}_{BIII} + \mathbf{e}_{III} \end{aligned} \quad (3.18)$$

The transition matrix is therefore

$${}^{III}M_{II^+} = \begin{bmatrix} 1 & t_3 - t_2^- \\ 0 & 1 \end{bmatrix}. \quad (3.19)$$

With the argument from the calculation of the mapping for the floor contact we would have to calculate a new intersection point of the hand trajectory with the ball trajectory. However, this case is already included in (3.19). This is because the linearization of the trajectories at the intersection point have the same state and derivative, we would only get a small additional time increment in element $\{1, 2\}$ of the matrix ${}^{III}M_{II^+}$ in (3.19). Since we suppose to have small errors we neglect this additional time increment.

Hand contact

By inserting the new initial conditions (3.18) at t_3 into (3.8) we obtain the perturbed solution for the hand contact. The linearization at t_{IV} yields

$${}^{IV}M_{III} = \begin{bmatrix} \cos(c\Delta t) & \frac{1}{K} \sin(c\Delta t) \\ -K \sin(c\Delta t) & \cos(c\Delta t) \end{bmatrix} \quad (3.20)$$

with $\Delta t = t_{IV} - t_{III}$ and $c = \sqrt{K_H/m_B}$.

Summary

Combining (3.11), (3.16), (3.19) and (3.20) we construct the mapping of the error e_{I_n} of cycle n to the initial error $e_{I_{n+1}}$ of the next cycle $n+1$ by multiplication of the error mapping matrices. This yields to the difference equation

$$e_{I_{n+1}} = \underbrace{{}^{IV}M_{III} \quad {}^{III}M_{II^+} \quad {}^{II^+}M_{II^-} \quad {}^{II^-}M_I}_{{}^{IV}M_I} e_{I_n}. \quad (3.21)$$

By analyzing whether the absolute value of the eigenvalues of the matrix ${}^{IV}M_I$ remains below 1 we can conclude the stability of the cycle. Together with the eigenvalues we also get an approximation of the convergence rate of the system.

In the following section we show how the ball can be tracked by a hybrid observer that relies on force sensing only and does not require additional vision information.

3.1.3 Ball Observer

In order to perform the dribbling task with a real robotic system it is important to be able to track the ball position. As we want to fully

exploit the capabilities of proprioceptive sensing in order to support e.g. a vision system with a very robust controller it can rely on, we use a nonlinear observer that is able to reliably track the ball based on contact forces only. Then, we give a stability proof for the observer over the full cycle, for which we assume that the ball is initially in contact with the elasticity (otherwise the system is unstable and no measurement would be available).

Observer structure

Since we are only measuring the forces acting during the contact phase, we lack a continuous measurement. Hence, we require an observer that converges in finite time during the contact phase. In [Dra92] a sliding mode observer is proposed, that satisfies our requirement. For a general nonlinear system of the form

$$\begin{aligned}\dot{\mathbf{x}} &= \mathbf{f}(\mathbf{x}), \quad \mathbf{x} \in \mathbb{R}^n \\ y &= h(\mathbf{x}), \quad y \in \mathbb{R},\end{aligned}\tag{3.22}$$

the observer

$$\dot{\hat{\mathbf{x}}} = \left(\frac{\partial \mathbf{H}(\hat{\mathbf{x}})}{\partial \mathbf{x}} \right)^{-1} M(\hat{\mathbf{x}}) \text{sgn}(\mathbf{V}(t) - \mathbf{H}(\hat{\mathbf{x}}))\tag{3.23}$$

with

$$\begin{aligned}\mathbf{H}(\mathbf{x}) &= [h(\mathbf{x}) \quad L_{\mathbf{f}}h(\mathbf{x}) \quad \dots \quad L_{\mathbf{f}}^{n-1}h(\mathbf{x})]^T \\ M(\hat{\mathbf{x}}) &= \text{diag}(m_1(\hat{\mathbf{x}}) \quad \dots \quad m_n(\hat{\mathbf{x}})) \\ \mathbf{V}(t) &= [v_1(t) \quad \dots \quad v_n(t)]^T\end{aligned}\tag{3.24}$$

is described. The coefficients v_i result from the available measurement and are defined as

$$\begin{aligned}v_1 &= y(t), \\ v_{i+1} &= m_i(\hat{\mathbf{x}}) \text{sgn}(v_i(t) - h_i(\hat{\mathbf{x}})), \quad i = 1(1)n - 1.\end{aligned}\tag{3.25}$$

[Dra92] provides a proof that the observer converges in finite time depending on the gain matrix $M(\hat{\mathbf{x}})$. With the force acting on the robot hand, its position, and the known spring stiffness of the hand we calculate the ball position and obtain the quantity y_B that acts as the observer input:

$$z_B(t) = \frac{F}{K_H} - r_B + z(t),\tag{3.26}$$

with F being the measured force. Therewith, the observer equation during hand contact is

$$\dot{\hat{\mathbf{z}}} = \mathbf{f}_2(\hat{\mathbf{z}}, t) + \left(\frac{\partial \mathbf{H}(\hat{\mathbf{z}})}{\partial \hat{\mathbf{z}}} \right)^{-1} M(\hat{\mathbf{z}}) \text{sgn}(\mathbf{V}(t) - \mathbf{H}(\hat{\mathbf{z}})).\tag{3.27}$$

For the ball being in the free flight phase, we use a prediction step based on the model equations shown in Fig. 2.4. The overall hybrid observer structure, represented as a directed graph is depicted in Fig. 3.3.

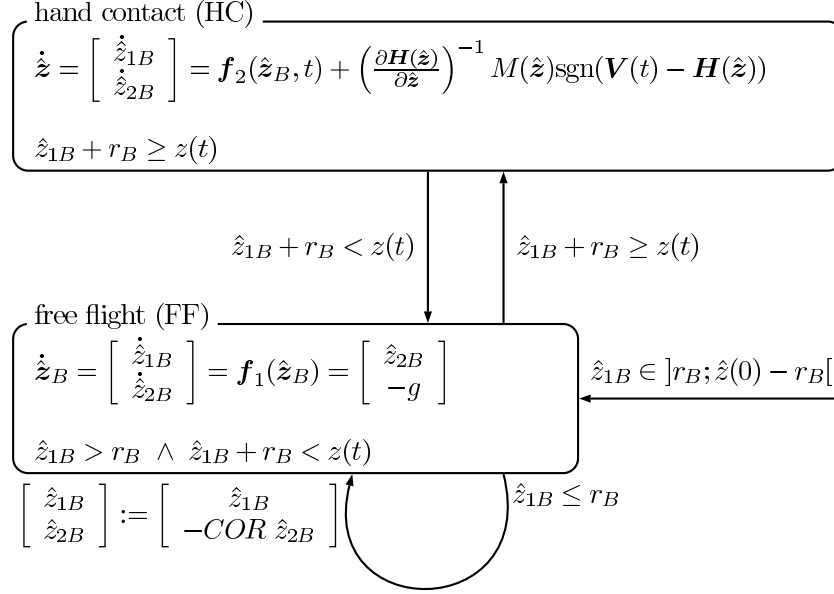


Figure 3.3: Directed graph of the ball observer.

In the next subsection we present a stability analysis of the hybrid observer for the entire dribbling cycle based on the Lyapunov stability definition (up to now only the convergence during contact phase is available).

Stability proof for the observer

For the observer stability we consider the typical ε, δ definition of Lyapunov stability that can be found in every standard nonlinear control textbook (e.g. [Kha02]).

Definition 2 (Lyapunov stability cf. [Kha02])

The equilibrium point $x = 0$ of (3.22) is

- stable if, for each $\varepsilon > 0$, there is $\delta = \delta(\varepsilon) > 0$ such that

$$\|x(0)\| < \delta \Rightarrow \|x(t)\| < \varepsilon, \forall t \geq 0. \quad (3.28)$$

As [Dra92] gives a proof for the finite time convergence of the sliding mode observer, it is sufficient to analyze only the time before hand contact for proving stability. The idea is to show the boundedness of

the error mapping during non-contact phase. For this we construct the ε, δ bounds that directly represent definition 2.

As we treat a linear system only, we may refer to the analysis from Sec. 3.1.2 for the evaluation of observer error dynamics. First, we obtain a mapping from the initial error (ball leaves hand contact) to the error at the start of the next hand contact by calculating

$$e_{III} = \underbrace{{}^{III}M_{II^+} \quad {}^{II^+}M_{II^-} \quad {}^{II^-}M_I}_{{}^{III}M_I} e_I. \quad (3.29)$$

Our interest in (3.29) is the mapping of balls at t_{III} (beginning of next hand contact) defined as

$$B_{III} = \{\mathbf{x} \in \mathbb{R}^2 \mid \|\mathbf{x}\|_2 \leq \varepsilon\} \quad (3.30)$$

back to t_I (ball leaves previous hand contact). Let us analyze the mapping of the border of B_{III} to t_I by building the scalar product of e_{III} with itself, defining that B_{III} is the border of e_{III} . This yields to

$$e_{III}^T e_{III} = e_I^T \underbrace{{}^{III}M_I^T \quad {}^{III}M_I}_{=: M_{obs}} e_I = \varepsilon^2 \quad (3.31)$$

Equation (3.31) with the matrix M_{obs} corresponds to a quadric that can be transformed by a main axis transformation to an ellipse E_I of the form

$$e_I^T \begin{bmatrix} \frac{1}{\varepsilon^2 a_1^2 (COR, t_{III}, t_{I^-}, z_{2B_{III}}^-)} & 0 \\ 0 & \frac{1}{\varepsilon^2 a_2^2 (COR, t_{III}, t_{I^-}, z_{2B_{III}}^-)} \end{bmatrix} e_I = 1, \quad (3.32)$$

where εa_1 and εa_2 are the lengths of the semi axes of the ellipse. Without loss of generality let εa_1 denote the smaller semi axis. Therewith, we can define a ball at t_I with

$$B_I = \{\mathbf{x} \in \mathbb{R}^2 \mid \|\mathbf{x}\|_2 \leq \varepsilon a_1\}, \quad (3.33)$$

which is a region at t_I . By mapping the border of this ball back to t_{III} via ${}^I M_{III}$, we construct an ellipse that lies inside B_{III} . This curve has two contact points at the major semi axis with the border of B_{III} . By taking the radius from B_{III} as ε and the radius from B_I as δ we get the function

$$\delta(\varepsilon) = \varepsilon a_1. \quad (3.34)$$

This approach is valid, as the region of the open set for B_I is a subset of the obtained ellipse from the first mapping of B_{III} . Furthermore, the open set resulting from the mapping from B_I forward is also a subset of B_{III} . Therefore, the system is stable.

Fig. 3.4 illustrates this approach. The left image shows the region of the circle B_{III} . For the given example we choose $\varepsilon = 1$. By mapping this

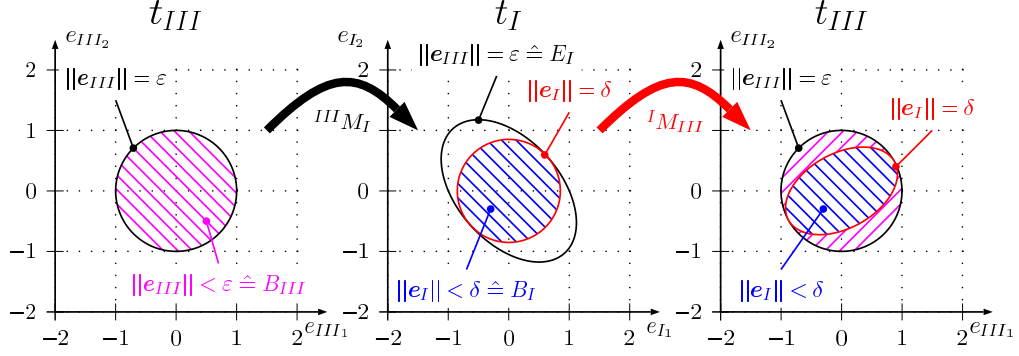


Figure 3.4: ε and δ regions for observer.

region forward via ${}^{III}M_I$ we obtain the black ellipse E_I (middle plot). The blue and red circle B_I is the inscribed circle of the ellipse and represents δ . By mapping this via ${}^I M_{III}$, we obtain the red and blue ellipse (right plot). Finally, the hatched, blue region lies completely in the black circle, which represents ε .

In the following section we present how the parameters for the hand trajectory are chosen.

3.1.4 Height Control

Until now we did not consider varying the parameters A, z_0 and T , which describe the hand trajectory. As it is not desirable to control all three simultaneously it would be useful to describe these parameters by a single variable. A possible choice would be the desired apex height of the ball or the desired impact velocity on the floor. However, interesting to notice is that all these basically refer to the ball energy and hence, we select the energy E_d after hand contact as a suitable variable.

The approach we choose for the period time T is depicted in Fig. 3.5. T is composed of

1. The time t_2 that a ball needs to fall from the apex height defined by the energy E_d .
2. The time t_1 for moving from the floor to the apex height is defined by the energy $COR^2 E_d$, which describes the energy after floor contact.

This time can be interpreted as the average over the two times derived from a floor to floor motion on the two energy levels E_d and $COR^2 E_d$. Therefore, an approximation for the period time.

From the simulations presented later in Chapter 4 it can be deduced that the remaining parameters A and z_0 are linearly depending on the

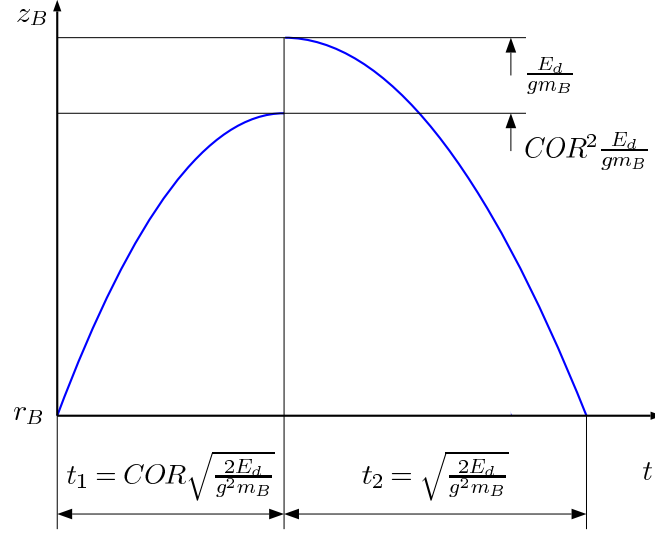


Figure 3.5: Calculation of the period time.

desired energy E_d . Hence, we make the ansatz

$$\begin{bmatrix} T \\ A \\ z_0 \end{bmatrix} = \begin{bmatrix} (COR + 1) \sqrt{\frac{2E_d}{g^2 m_B}} \\ A_1 + A_2 E_d \\ z_{01} + z_{02} E_d \end{bmatrix} \quad (3.35)$$

with A_1, A_2, z_{01} and z_{02} as constants that are to be found.

Unfortunately, a proof for the correctness of this parameter choice is still to be done. However, a clear hint is given by the energy of the hand trajectory. This can be found to be

$$E_H = m_B g \left(\underbrace{z_0}_{\sim E_d} + \underbrace{A \sin(\omega t)}_{\sim E_d} \right) + \frac{1}{2} m_B \underbrace{\left(\underbrace{A \omega \cos(\omega t)}_{\sim \frac{E_d}{\sqrt{E_d}}} \right)^2}_{\sim E_d}. \quad (3.36)$$

Hence, with the chosen hand trajectory parameters (3.35) the hand trajectory behaves proportional to the desired energy.

For changing the desired energy online we filter the amplitude A and the height z_0 by a PT2-element. This leads to two times continuous differentiability. The period time T is also filtered by a PT2, but is used as a discrete variable that is updated in the trajectory generator at every period start. Furthermore, we use a discrete PID control as an additional summand ΔA on the amplitude with the energy error ΔE as an input, which is [Lun06b]

$$\Delta A_n = K_P \Delta E_n + K_D (\Delta E_{n-1} - \Delta E_n) + K_I \sum_{i=0}^n \Delta E_i \quad (3.37)$$

with K_P, K_D and K_I as control parameters.

3.1.5 Summary

In Fig. 3.6 the block diagram of the control for the 1 DoF model is depicted. The desired Energy E_d is the input. The hand trajectory z is calculated from (2.6) and (3.35) in Σ_{Traj} . Besides Σ_{Traj} is also fed with ΔA from the height control (3.37). G represents the model with the ball state z_B and the measured force F as respective output. F is fed into the observer Σ_{Obs} , from which we obtain the energy level after hand contact. This, in turn, is used in the PID for the hand amplitude.

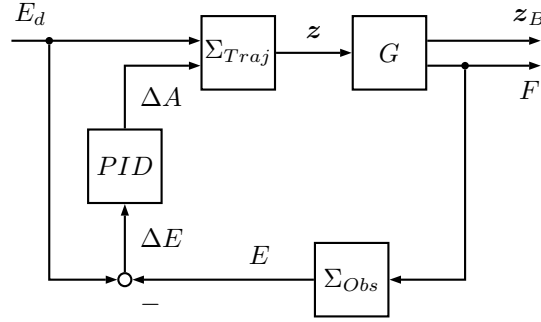


Figure 3.6: Overall block diagram of the 1 DoF controller structure.

3.2 3 DoF Model

For the control of the vertical motion of the 3 DoF model we use the same structure as for the 1 DoF model. vertical motion. Hence, we present only the extension for the horizontal motion.

3.2.1 Observer

For the additional translational DoF we can use the same prediction observer structure as for the 1 DoF case. Hence, the position of the ball from the measured reaction forces needs to be calculated. These can be obtained by using (A.22) and the Newton-Euler equations from Sec. 2.2, which yields

$$\mathcal{G} = \begin{bmatrix} F_x \\ F_z \\ F_y \end{bmatrix} = \begin{bmatrix} m_H \left(\frac{1}{2} \dot{\beta}^2 l_H \cos(\beta) + \frac{d^2 x(t)}{dt^2} \right) \\ -F_{HC_n} \sin(\beta) - F_{HC_t} \cos(\beta) \\ m_H \left(-\frac{1}{2} \dot{\beta}^2 l_H \sin(\beta) + \frac{d^2 z(t)}{dt^2} \right) + m_H g \\ + F_{HC_t} \sin(\beta) - F_{HC_n} \cos(\beta) \\ K_H(\alpha(t) - \beta) \end{bmatrix}. \quad (3.38)$$

In (3.38) F_x and F_z denote the reaction forces in x and z direction and F_y the reaction moment about the y axis.

The ball contact position is denoted by δ and has to be calculated from (2.38). The required hand contact force F_{HC_n} can then be calculated with the ansatz

$$F_x \sin(\beta) + F_z \cos(\beta), \quad (3.39)$$

which yields

$$F_{HC_n} = -F_x \sin(\beta) - F_z \cos(\beta) + m_H \left(\frac{d^2 x(t)}{dt^2} \sin(\beta) + \frac{d^2 z(t)}{dt^2} \cos(\beta) + g \cos(\beta) \right). \quad (3.40)$$

For the calculation of F_{HC_n} the deflection of the spring β via an observer needs to be obtained. However, the real 6 DoF model does not have a spring with mass and thus, does not require such an observer. Hence, we take β and its derivatives for granted. This yields the ball position used for the ball observer

$$\mathbf{x}_B^{obs} = \begin{bmatrix} x(t) - \delta \cos(\alpha) - r_B \sin(\alpha) \\ 0 \\ z(t) + \delta \sin(\alpha) - r_B \cos(\alpha) \end{bmatrix}. \quad (3.41)$$

Therewith, we can use the same observer as in the 1 DoF model for the vertical and the horizontal translation. Until now the rotation is not taken into account for the observer.

3.2.2 Control

For the ball height control we use the scheme from Sec. 3.1.4. Hence, we discuss only the control of the vertical ball motion in this section, leaving only two remaining DoF are left in the hand.

It is obvious that we have to track the vertical ball position with the vertical hand position, as otherwise no hand contact would be present and, hence, no stable dribbling would be possible. The desired vertical position of the hand is

$$x_d = \hat{x}_B + \delta_x, \quad (3.42)$$

with the observed position \hat{x}_B , and δ_x being an offset so that the ball is kept at the middle of the finger.

With the remaining DoF we want to drive the ball to a steady state x_{B_d} . Therefore, we use a PID controller with the following structure:

$$\begin{aligned} \alpha_d = & K_{P\alpha}(x_d - \hat{x}_B(t)) \\ & + K_{I\alpha} \int_0^t (x_d - \hat{x}_B(\tau)) d\tau \\ & + K_{D\alpha}(\dot{x}_d - \dot{\hat{x}}_B(t)), \end{aligned} \quad (3.43)$$

with $K_{x\alpha}$ as control parameters. The α_d signal is filtered by a PT2 element for obtaining twice continuous differentiability.

3.2.3 Summary

In Fig. 3.7 the overall block diagram of the control structure is depicted. Basically, it is the same closed loop as in Sec. 3.1.5 for the desired energy E_d . In addition, the observer provides the vertical position \hat{x}_B , which is used for the vertical position, cf. (3.42), and the rotation, cf. (3.43).

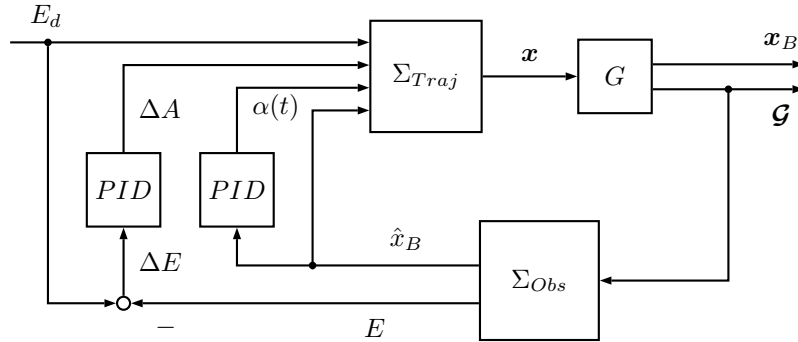


Figure 3.7: Overall block diagram of the 3 DoF model controller structure.

In the following section we present the 6 DoF control structure.

3.3 6 DoF Model

As outlined in Sec. 2.3 we use a full dynamic flexible joint model for the robot and also the full 6 DoF for the ball. Therefore, we present first an observer for the translational DoF of the ball and then the used control. At the end of this section the Cartesian impedance control for the LWR III is shortly summarized.

3.3.1 Observer

The observer structure presented in Sec. 3.1.3 is used for all three translational DoFs. For this we have to obtain the ball position from the measured forces. This measurement is obtained by a JR3 6 DoF force/torque sensor [JR3] mounted in the robot wrist. Since this signal is overlaid by noise, forces due to the acceleration of the hand mass, and also the oscillating springs we have to correct this signal. In the following, we first show how the position is obtained and then how the signal is filtered.

Since we assume negligible contact moments, we can use the principle of solidification for calculating the ball position, i.e. there has to be a straight line on which no moments are acting [MMS05]. This straight

line ${}^{EE}\mathbf{r}_S(\lambda)$ can be found by solving

$${}^{EE}\mathbf{M}_{ext} = {}^{EE}\mathbf{r}_S(\lambda) \times {}^{EE}\mathbf{F}_{ext} \quad (3.44)$$

for ${}^{EE}\mathbf{r}_S(\lambda)$, with λ being the curve parameter of the straight line. Therewith, the contact point ${}^{EE}\mathbf{r}_c$ is obtained from the intersection of ${}^{EE}\mathbf{r}_S(\lambda)$ with the finger plane ${}^{EE}x = -\delta_x$. ${}^{EE}\mathbf{M}_{ext}$ is the measured contact moment and ${}^{EE}\mathbf{F}_{ext}$ the measured force vector. With ${}^{EE}\mathbf{r}_C$ and (2.60) we obtain the reflected stiffness at the contact point. Hence, with the direction of the straight line, which is given by ${}^{EE}\mathbf{F}_{ext}$ the ball position position is

$${}^{EE}\mathbf{r}_B = {}^{EE}\mathbf{r}_C + \frac{{}^{EE}\mathbf{F}_{ext}}{|{}^{EE}\mathbf{F}_{ext}|} \left(-r_B + \frac{|{}^{EE}\mathbf{F}_{ext}|}{K({}^{EE}\mathbf{r}_C, E, I_y)} \right). \quad (3.45)$$

This quantity takes the ball radius r_B and the spring bending into account. As the sliding mode observer tends to scattering, we filter the observed ball position with a PT3 element prior to using it in the feedback loop (see Sec. 3.3.2). Therewith, we get a reference that is three times continuously differentiable, i.e. only jerk scatters.

The measured force signal contains not only contact forces, but also high frequency noise, disturbances due to the oscillations of the intrinsically compliant fingers, and inertial effects of the load seen by the sensor while performing the dribbling motion. Therefore, we need to compensate the most significant effects for reliably estimating the contact position of the ball. In order to eliminate the high-frequency noise, we simply filter the raw signal with a PT2 element. As the finger oscillations have only a small amplitude and the associated frequency is very close to the frequency spectrum of the contact force, we neglect this effect. Because the desired dribbling motion demands very high acceleration, inertial forces due to the load mass are the most significant disturbance. Since acceleration cannot be obtained from currently available position sensors via twice numerical differentiation, we need an appropriate method to observe the Operational space acceleration of the robot flange.

In order to get a reliable acceleration estimate, we use a nonlinear disturbance observer according to [Had11]. It is defined as

$$\hat{\mathbf{q}} = M^{-1}(\boldsymbol{\tau} - \mathbf{n}(\mathbf{q}, \dot{\mathbf{q}}) - K_O(\hat{\mathbf{q}} - \dot{\mathbf{q}})), \quad (3.46)$$

where $\hat{\mathbf{q}}$ denotes the observed joint position, $\mathbf{n}(\mathbf{q}, \dot{\mathbf{q}}) = C(\mathbf{q}, \dot{\mathbf{q}})\dot{\mathbf{q}} + \mathbf{g}(\mathbf{q})$, and K_O is the observer gain matrix. With this we get an observation of $\ddot{\mathbf{q}}$ that relies on the measurement of the joint position and velocity only. Figure 3.8 depicts the according signal flow diagram.

With the observed joint accelerations $\hat{\mathbf{q}}$ we can easily obtain the Cartesian accelerations and consequently also the forces due to load accelerations via

$$\hat{\mathbf{x}} = \mathbf{J}\hat{\mathbf{q}} + \dot{\mathbf{J}}\hat{\mathbf{q}}. \quad (3.47)$$

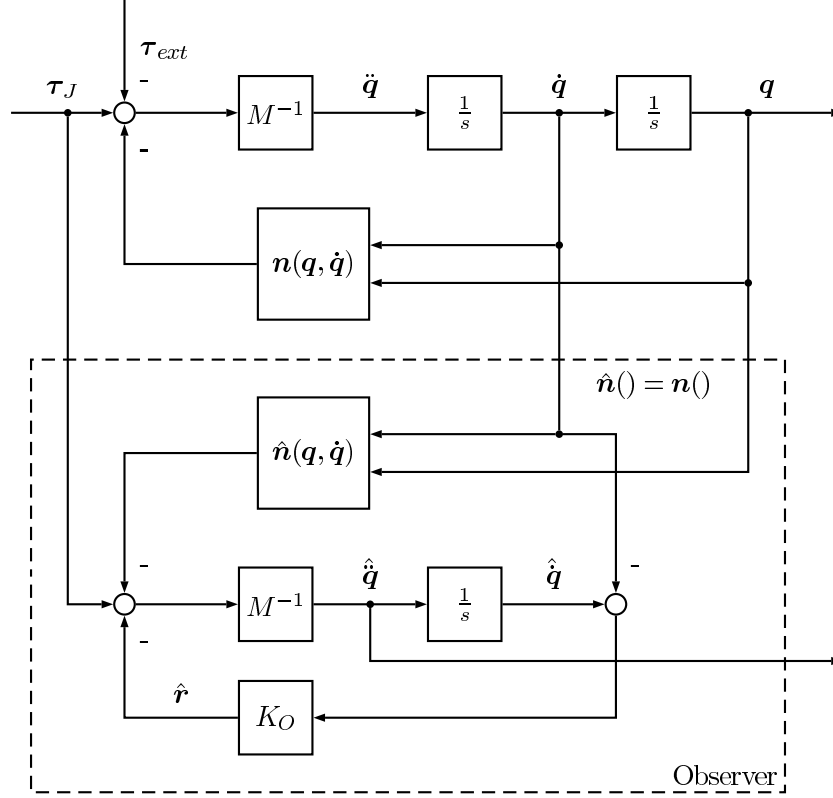


Figure 3.8: Velocity disturbance observer.

3.3.2 Control

In general, we intend to stabilize the ball at a steady point x_{B_d} (in fact at a projection on the horizontal plane). For the vertical motion we refer to the methods presented in Sec. 3.1.4. For stabilizing the lateral motion, the hand needs to follow the observed ball position from Sec. 3.3.1. Since we want to control the ball in cylindrical coordinates (see Fig. 2.7), the desired position is

$$\begin{bmatrix} x_d \\ y_d \\ \varphi_d \end{bmatrix} = \begin{bmatrix} -(d_B - \delta_H) - \sin(\varphi_B) \\ (d_B - \delta_H) \cos(\varphi_B) \\ \varphi_B \end{bmatrix}, \quad (3.48)$$

with δ_H being an offset from the $\{EE\}$ coordinate system to the middle of the finger. For attracting the ball to x_{B_d} we use a simple PID control for the two remaining hand rotations:

$$\begin{aligned} \beta_d &= K_{P\beta}(d_{B_d} - d_B(t)) \\ &\quad + K_{I\beta} \int_0^t (d_{B_d} - d_B(\tau)) \mathrm{d} \tau \\ &\quad + K_{D\beta}(\dot{d}_{B_d} - \dot{d}_B(t)), \end{aligned} \quad (3.49)$$

$$\begin{aligned}
\gamma_d &= K_{P\gamma}(\varphi_{B_d} - \varphi_B(t)) \\
&+ K_{I\gamma} \int_0^t (\varphi_{B_d} - \varphi_B(\tau)) d\tau \\
&+ K_{D\gamma}(\dot{\varphi}_{B_d} - \dot{\varphi}_B(t)),
\end{aligned} \tag{3.50}$$

with K_{xx} being the respective gains for the PID control.

In the following the Cartesian impedance control that is used for the robot control is explained in more detail.

3.3.3 Cartesian impedance control

Based on the elastic joint model described in Sec. 2.3.5 a cascaded control structure is used. The inner control loop is closed about the motor dynamics given by (2.67). For this the LWR III has torque sensors integrated in the joints. The outer control loop implements the Cartesian impedance control on the robot dynamics given by (2.66). An Overview on this can be found in [ASOH07].

Joint torque control

The joint torque control for the LWR III is presented in [OASK⁺04]. An exact linearization is applied on (2.67) by choosing a new input v for the system, which yields a Brunovsky normal form [Kha02]

$$v = \ddot{\theta}. \tag{3.51}$$

This is obtained by choosing the motor torque as

$$\tau_m = Bv + \tau + DK^{-1}\dot{\tau} = Bv + \tau_a. \tag{3.52}$$

For the double integrator in (3.51) [OASK⁺04] proposes the desired dynamical system

$$B_\theta \ddot{\theta} + \tau + D_S K^{-1} \dot{\tau} = u \tag{3.53}$$

with a new diagonal motor inertia matrix B_θ and a new diagonal gain matrix for the derivative feedback D_S . This leads to the feedback for the Brunovsky normal form (3.51)

$$v = B_\theta^{-1} (u - \tau - D_S K^{-1} \dot{\tau}). \tag{3.54}$$

Hence, we obtain the overall torque feedback by inserting (3.54) into (3.52), which yields

$$\begin{aligned}
\tau_m &= BB_\theta^{-1}u + \tau_a \\
&- BB_\theta^{-1}(\tau + D_S K^{-1}\dot{\tau}).
\end{aligned} \tag{3.55}$$

With this control law, a PD torque controller is implemented for each joint. Its benefit is that the desired motor inertia and the derivative feedback can be chosen freely. In practice a value between 4 and 6 is selected for the ratio BB_θ^{-1} [ASOH07].

Cartesian impedance control

Impedance control was first mentioned by [Hog85]. The extension of this control framework to a passivity based Cartesian impedance control was made in [ASOH04]. With [Hog85] we may choose an outer loop controller to be, cf. [ASOH07],

$$\mathbf{u} = -J(\mathbf{q})^T(K_x\tilde{\mathbf{x}}(\mathbf{q}) + D_x\dot{\mathbf{x}}) + \mathbf{g}(\mathbf{q}) \quad (3.56)$$

with $J(\mathbf{q})$ being the manipulator Jacobian and $\tilde{\mathbf{x}} = \mathbf{x} - \mathbf{x}_d$ which is the Cartesian error of the desired position \mathbf{x}_d and the current position \mathbf{x} . \mathbf{x} is calculated by the forward kinematics $\mathbf{x} = \mathbf{f}(\mathbf{q})$ and $\mathbf{g}(\mathbf{q})$ is a gravity compensation term for the static case.

The dynamical system of the robot (2.66)-(2.69) is passive to its pair of inputs and outputs $\{\boldsymbol{\tau}_a + \boldsymbol{\tau}_{ext}, \dot{\mathbf{q}}\}$ with the storage function $S_q = 1/2\dot{\mathbf{q}}^T M(\mathbf{q})\dot{\mathbf{q}} + V_g(\mathbf{q})$ where V_g is a potential function dependent on the $\mathbf{g}(\mathbf{q})$. However, it lacks this property when using the prementioned control law (3.56). Generally passivity is a property that is desirable, as it also leads to stability. To achieve it, a one to one mapping of the motor side and link side positions at equilibrium points $\boldsymbol{\theta}_0$ and \mathbf{q}_0 is used, which is given by [ASOH07]

$$\boldsymbol{\theta}_0 = \mathbf{h}(\mathbf{q}_0) = \mathbf{q}_0 + K^{-1}\mathbf{l}(\mathbf{q}_0) \quad (3.57)$$

$$\text{with } \mathbf{l}(\mathbf{q}_0) = -J(\mathbf{q}_0)^T K_x \tilde{\mathbf{x}}(\mathbf{q}_0) + \mathbf{g}(\mathbf{q}_0). \quad (3.58)$$

With this mapping The joint positions \mathbf{q} in (3.56) can be replaced by the motor side positions $\boldsymbol{\theta}$ together with the inverse mapping of (3.57) $\bar{\mathbf{q}}(\boldsymbol{\theta}) = \mathbf{h}^{-1}(\boldsymbol{\theta})$. This yields

$$\mathbf{u} = -J(\bar{\mathbf{q}})^T(K_x\tilde{\mathbf{x}}(\bar{\mathbf{q}}) + D_x J(\bar{\mathbf{q}})\dot{\boldsymbol{\theta}}) + \mathbf{g}(\bar{\mathbf{q}}) \quad (3.59)$$

with $\tilde{\mathbf{x}} = \mathbf{f}(\bar{\mathbf{q}}) - \mathbf{x}_d$. Furthermore, the velocity in the derivative part of (3.56) is also replaced by its equivalent on the motor side position. In the static case (3.59) and (3.56) are equivalent. Now (3.59) leads to the desired passivity property with respect to $\{\dot{\boldsymbol{\theta}}, -\mathbf{u}\}$.

This control is implemented on the LWR III running at a rate of 1 kHz. In the basketball case we further use a velocity feed forward term in the derivative part of (3.59), to achieve a better tracking performance. In this thesis we use $K_x = \text{diag}\{1500 \ 1500 \ 1500 \ 200 \ 200 \ 200\}$ (translational stiffness in N/m and rotational stiffness in Nm/rad).

3.3.4 Summary

Figure 3.9 depicts the overall structure of the controller. We use the same control loop for the desired energy E_d as in Sec. 3.1.4. Furthermore, we feed the observed ball position $\hat{\mathbf{x}}_B$ into the trajectory generator, which is used for ball tracking, cf. (3.48). $\hat{\mathbf{x}}_B$ is also used for the PID control that is acting on the two rotations β_d, γ_d . the force signal for the observer is filtered by Σ_{fil} .

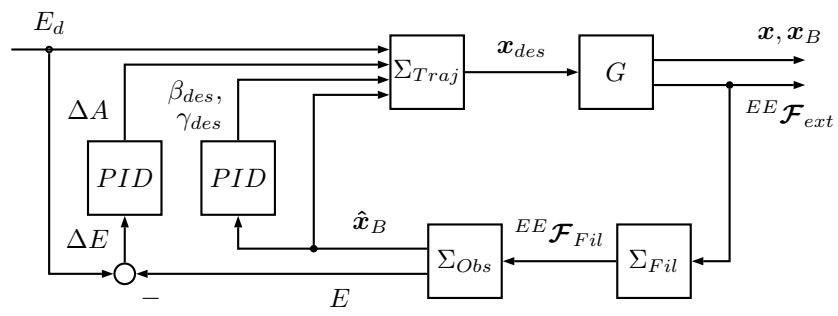


Figure 3.9: Overall block diagram of the 6 DoF control structure.

4

Simulations and Experiments

Until now we described the used models and the control for achieving a stable dribbling robot. In this chapter we show results obtained from simulations and experiments. As there is no straight forward way to obtain the constraints acting on the ball in reality, we show only full DoF experiments. However, in order to understand the effect of the controllers on the reduced DoF problem, the simulation results are described first and then measurements obtained from experiments with an LWR III and an unconstrained ball. Overall, the proposed control laws ensure very robust and stable elastic dribbling.

4.1 Simulations

In the following some results obtained from simulations are presented.

4.1.1 1 DoF Model

A sample simulation is shown in Fig. 4.1. The black plot depicts the hand trajectory z , which is displaced by an offset $-r_B$, so that the hand contact becomes clear. During the first 0.5 s we use a 5th order polynomial to reach the stimulating trajectory (2.6). The blue curve depicts the ball motion z_B . It starts after the 0.5 s lasting starting motion of the hand. From looking at the apex height it becomes clear that the ball stabilizes its height after some cycles. The dashed red plot denotes the ball observer position \hat{z}_B . Its initial position is set to the ball position, while its velocity has a significantly larger value than the true ball velocity. Despite this significant initial discrepancy, it can be

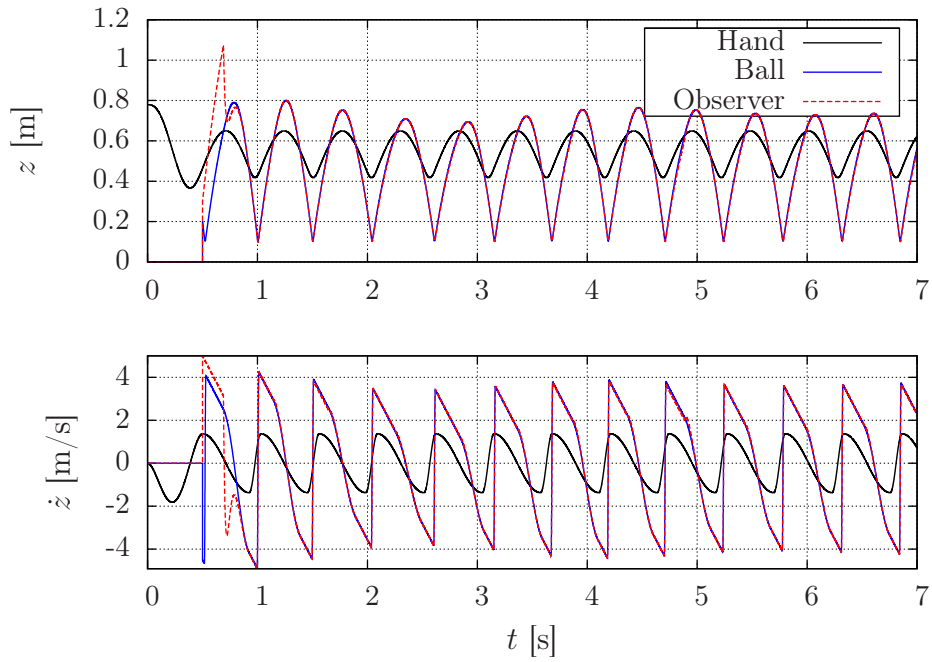


Figure 4.1: Position and velocity for the ball, ball observer and hand in a simulation with the 1 DoF Model. The hand is initialized by a polynomial in the first 0.5 s. The ball and observer are started after this time.

seen that the observer converges during the first contact phase.

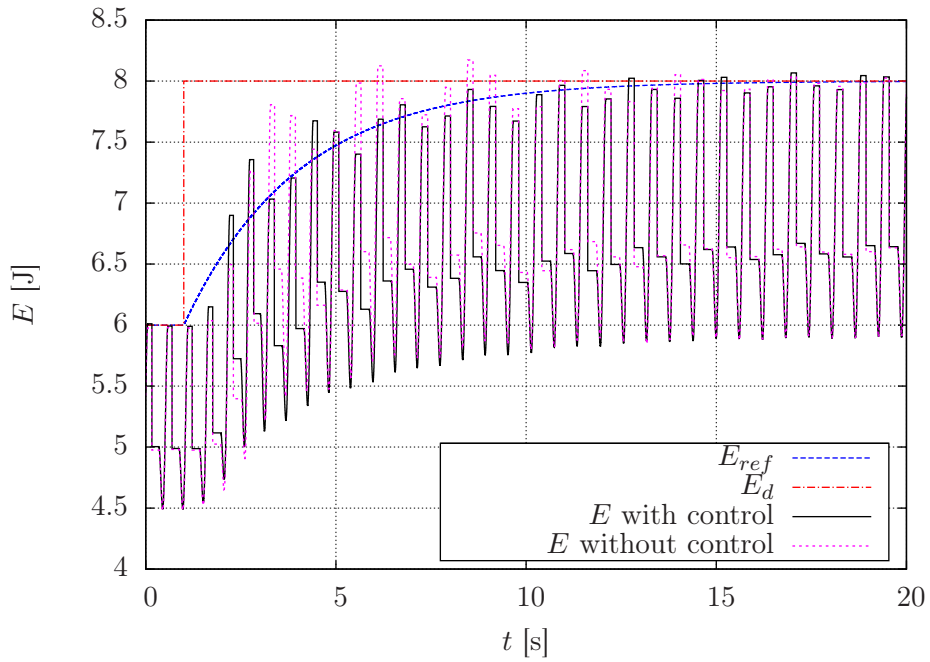


Figure 4.2: Energy for the simulation of the 1 DoF Model with and without PID control for the height. After 1 s a step is performed in the reference Energy from 6 J to 8 J.

In Sec. 3.1.4 we described a control structure for the dribbling height. A sample simulation for such a reference change in the desired energy is depicted in Fig. 4.2. There, we see the reference energy marked red. At $t = 1$ s a step from $E_d = 8$ J to $E_d = 10$ J is performed. The blue trajectory depicts the PT 1 filtered reference energy that is used for the parameters as we do not want to have fast changes in the parameter signal. With the given continuous control law these certainly lead to instability due to the loss of hand contact. In magenta and black two ball trajectories are depicted. The magenta one is the model without additional PID control (3.37) acting on the amplitude, the other one with. From this, we see that the performance with and without control is nearly the same. However, the clear benefit of using control is the convergence due to the integral part. Furthermore, the used parameters for the height control are deduced from simulation and certainly not perfect.

4.1.2 3 DoF Model

Figure 4.3 depicts the resulting ball, observer, and hand motion for the 3 DoF model. In the upper plot the lateral position is shown. The steady state point of the ball is located at $x_B = 0$. The shift of the hand plot with respect to the ball plot is founded in the fact that the position of the bearing is plotted. Clearly, the ball stabilizes at the desired position. In the lower plot the vertical position is depicted. Also in this direction we obtain a stable cycle for the ball motion. Furthermore, we see that the observer converges within two cycles towards the true ball trajectory. Even though we have a rotational and not a translational spring in this model the vertical motion is very similar to the one from Fig. 4.1. Please note that in Fig. 4.1 the hand trajectory is translated downward by the ball radius to visualize the contact. This is less meaningful because of the rotation of the hand in the 3 DoF model.

4.1.3 6 DoF Model

The simulation results in this subsection consider the full dynamic model of the LWR-III (see Sec. 2.3.5) that is controlled via Cartesian impedance control (see Sec. 3.3.3).

Figure 4.4 depicts the ball and hand position expressed in $\{W\}$, again for a regulation dribbling task, however, for a full simulation of robot and impedance controller. Please note that the same y -axis offset as for the 3-DoF simulation is present. As one can see the motion converges quickly to the desired stable dribbling cycle in all three axes. Figure 4.5 shows the contact forces expressed in $\{EE\}$. The maximal contact force is ≈ 20 N along the x -axis. The forces in the z -axis are caused by the ball friction.

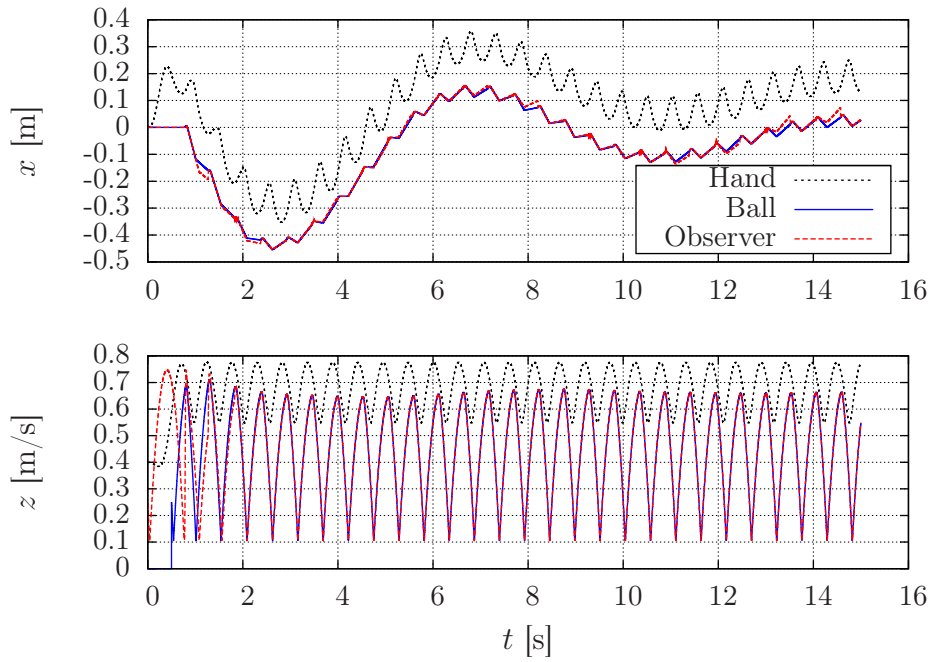


Figure 4.3: Position of the ball, ball observer and robot hand in a simulation with the 3 DoF Model. The ball and observer are started after the 0.5 s lasting initialization trajectory of the hand.

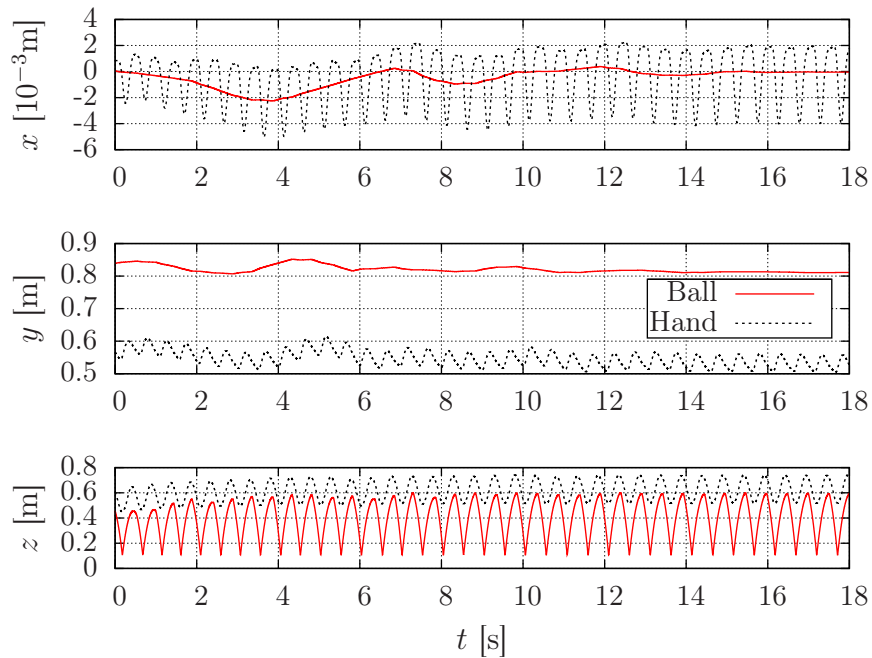


Figure 4.4: Positions of the ball and hand of a sample simulation of the 6 DoF model.

Figure 4.6 shows that it is possible also to vary the lateral set-point and desired distal point online. A change in the reference is per-

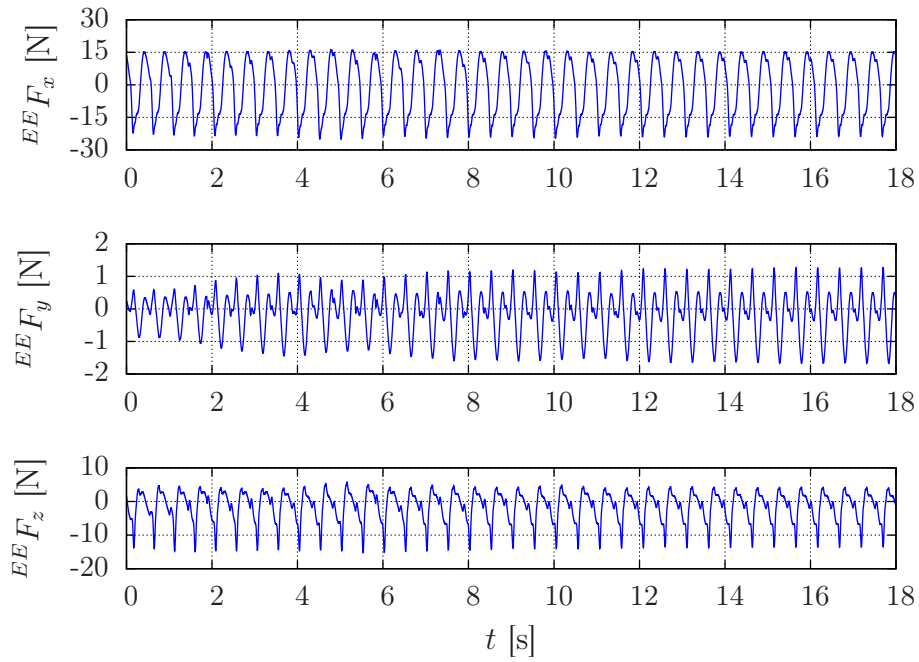


Figure 4.5: Measured and filtered forces in the hand. The impact force can be seen in the x direction. The forces in the z direction are evoked by the friction of the ball during contact.

formed, therefore, at $t = 31$ s from $[d_B \ \varphi_B]^T = [0.84 \text{ m} \ 0]^T$ to $[d_B \ \varphi_B]^T = [0.77 \text{ m} \ \pi/4]^T$. In other words, with the designed controller the robot is able to follow a desired dribbling trajectory $[d_B(t), \varphi_B(t)]$ without destabilization.

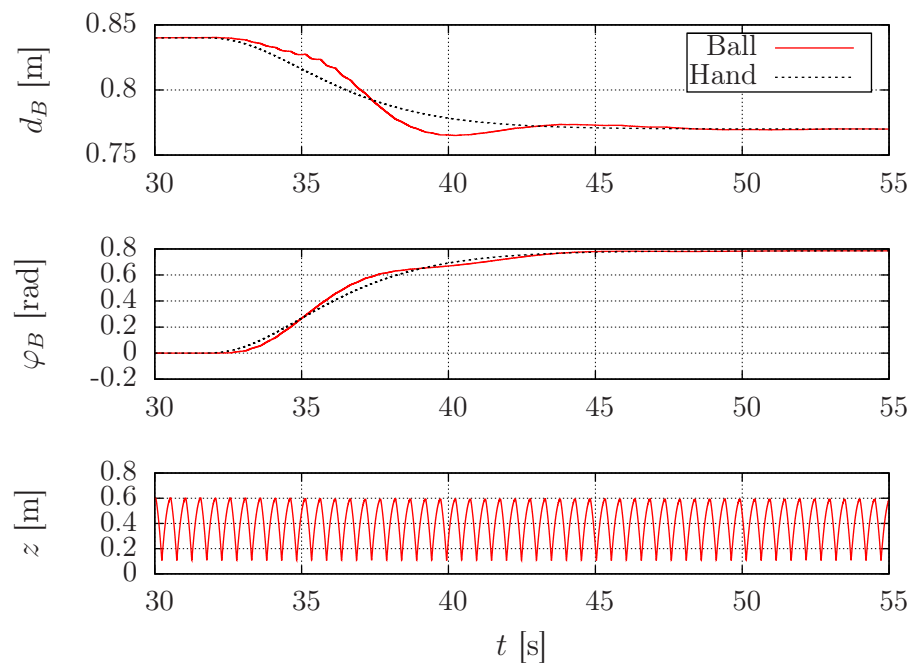


Figure 4.6: Cylindrical coordinates for the ball and hand in a sample simulation of the 6 DoF model. At $t = 31$ s a reference change of the dribbling position is performed from $[d_B \ \varphi_B]^T = [0.84 \text{ m} \ 0]^T$ to $[d_B \ \varphi_B]^T = [0.77 \text{ m} \ \pi/4]^T$.

4.2 Experiments

In this section we present experimental results for dribbling with a Cartesian impedance controlled LWR III. Due to time reasons, some conceptual features developed in this thesis and verified in all simulations were not fully transferred to the full experimental system. Nonetheless, the successful regulation dribbling shows very promising results. The missing features in the experimental control, observation of the vertical motion, cf. Sec. 3.1.3, and the height control, cf. Sec. 3.1.4 will be included in a near future work.

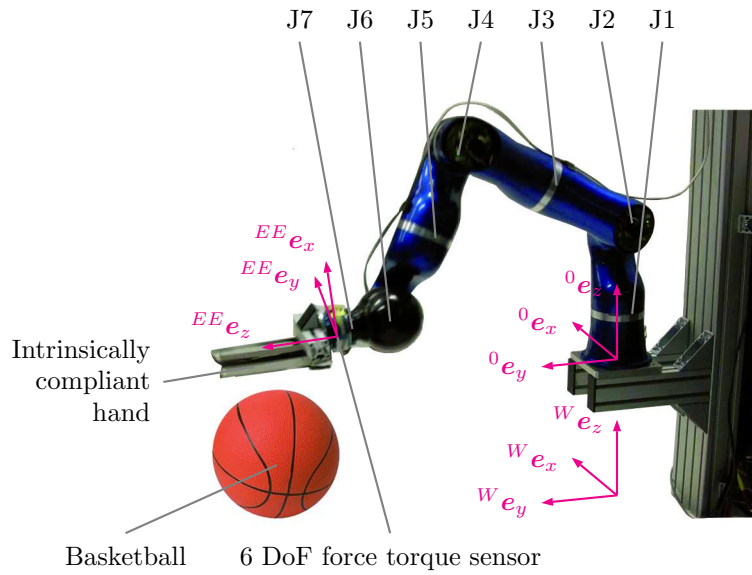


Figure 4.7: Experimental setup for basketball dribbling with the LWR III.

In Fig. 4.7 the experimental setup is depicted. The seven revolute joints of the LWR III are denoted by J1 - J7. The three coordinate systems are world $\{W\}$, base $\{0\}$ and end effector $\{EE\}$. They are placed according to the 6 DoF model, cf. Fig. 2.7. Hence, the robot base is collinear with the world frame and parallel to the floor. This configuration is very suitable for our control approach: The vertical motion is mainly performed by the joints 2, 4 and 6. The tracking of the ball in cylindrical coordinates is mainly performed by joint 1 for the angle φ_B and joints 2, 4 and 6 for the radius d_B . The remaining rotations for the control β_d and γ_d are mainly done joints 6 and 7.

The JR3 6 DoF force-torque sensor and the dribbling hand are directly mounted to the robot flange.

The electronics of the robot as e.g. power electronics and sensors is

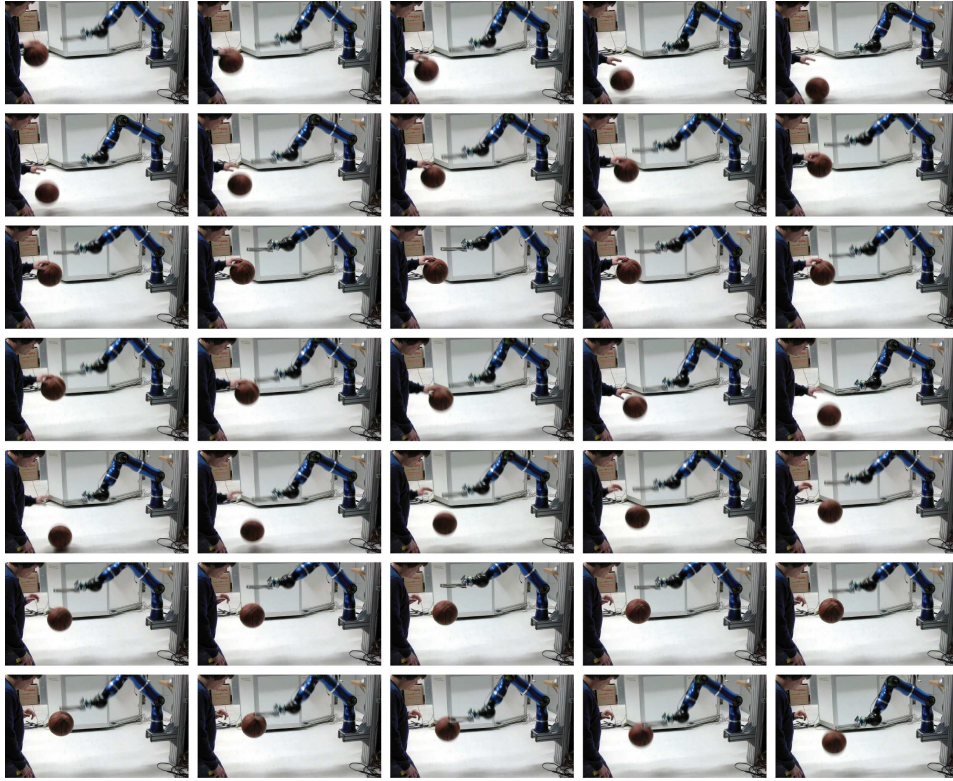


Figure 4.8: Image series of ball initialization. The time difference between two pictures is $1/24 \text{ s} \approx 41,7 \text{ ms}$.

completely integrated articulated structure. Overall, the manipulator needs only 24 V voltage as current supply. The real-time control operating the low-level control and also the dribbling control runs on a VxWorks [Riv] computer at a computation rate of 1 kHz. As already mentioned the robot has seven joints and, hence, one additional DoF apart from the ones that are needed to provide the three positions and three rotations of the end effector. In Operational space control (e.g. Cartesian impedance control) this additional DoF can be described in terms of the nullspace of the task Jacobian, cf. [Ott08]. In our case it is controlled by a virtual force acting on the elbow of the robot that points upwards.

At the start and the end of the robot motion we use a 5th degree polynomial to reach vertical trajectory (2.6) and the end steady state respectively. The observed ball starts motionless lying on the ground at the starting position of the robot. To get the dribbling cycle started a human dribbles manually the ball into the dribbling motion of the robot. In Fig. 4.8 an image series for bringing the ball into the dribbling process is depicted.

Figure 4.9 shows an image series of successful elastic dribbling cycles with the LWR III. The utilization of the elastic fingers can be clearly observed. In Fig. 4.10 an image series from a front view of a successful

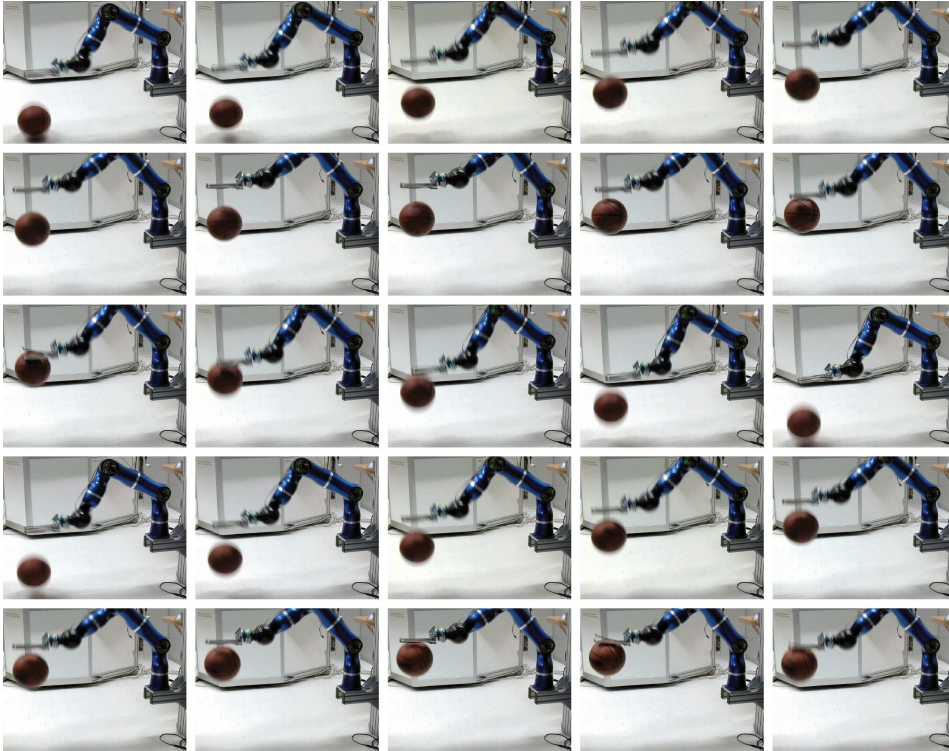


Figure 4.9: Image series of a successful dribbling cycle. The time difference between two pictures is $t = 1/24 \text{ s} \approx 41.7 \text{ ms}$.

dribbling cycle is depicted. In the beginning, the hand is not centered above the ball. It can be seen that over the image series the hand centers by moving to the right above the ball, thus maintaining a stable dribbling cycle.

A sample measurement of the dribbling is depicted in Fig. 4.12 and Fig. 4.11. In the first figure the ball position is shown in cylindrical coordinates d_B and φ_B respectively. In the second figure the disturbance compensated end-effector forces are visualized. The maximal force in the upper plot is in a similar range as for the 6 DoF simulation, see Fig. 4.5. Furthermore, the finger oscillations can be observed mainly in x -direction of $\{EE\}$. Overall, the robot is able to quickly stabilize the ball motion.

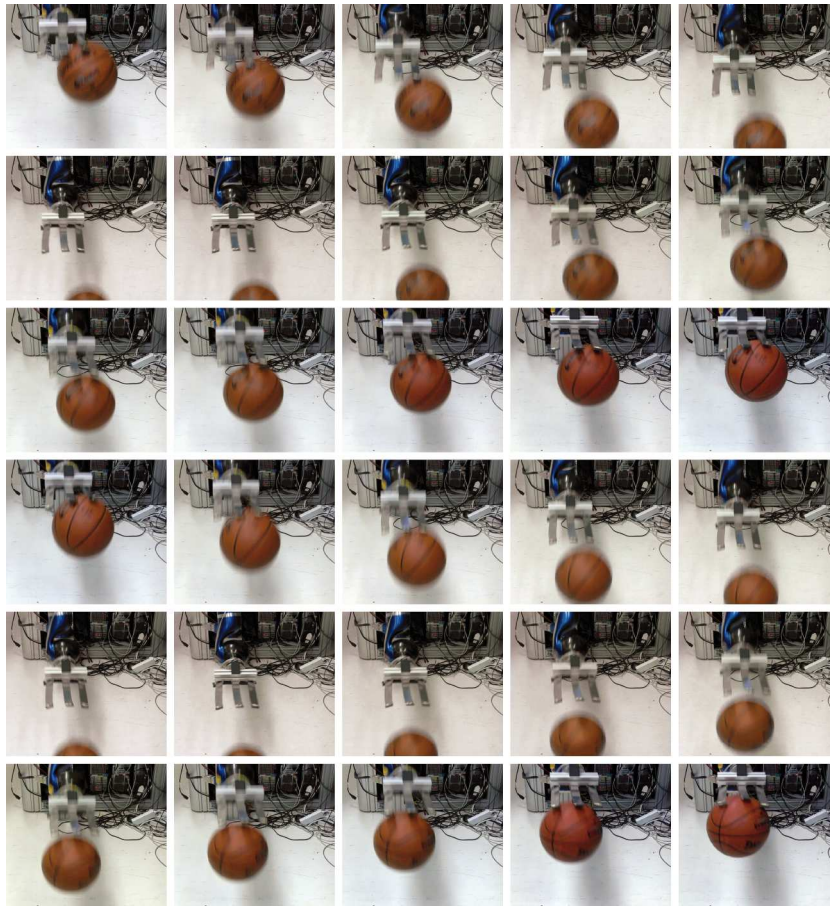


Figure 4.10: Front view series of a successful dribbling cycle. The time difference between two pictures is $t = 1/24 \text{ s} \approx 41.7 \text{ ms}$.

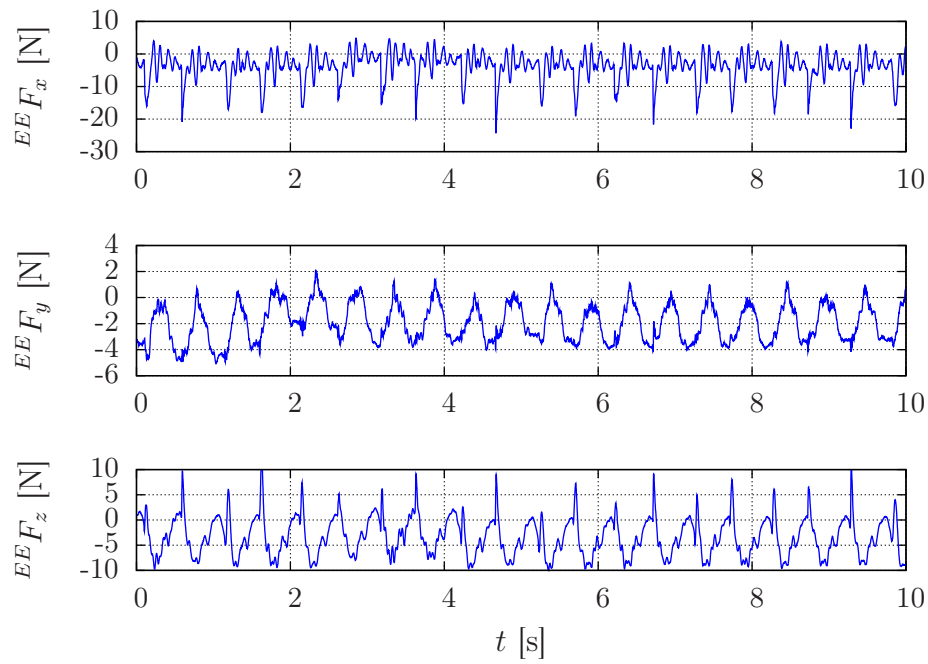


Figure 4.11: Measured and filtered forces for the hand contact from which the positions are obtained.

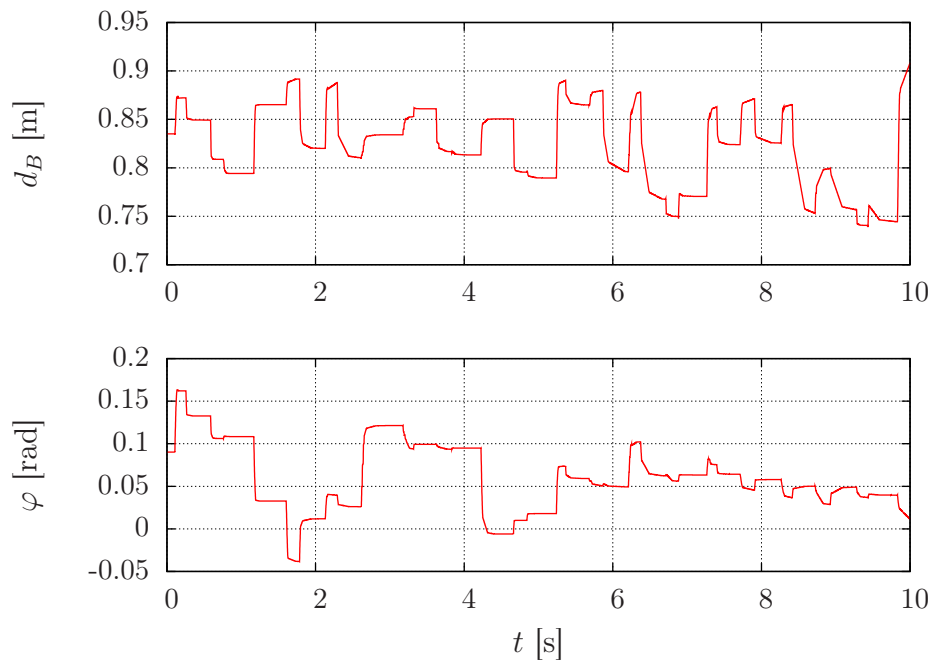


Figure 4.12: Observed position of the ball for a sample measurement in an experiment.

5

Conclusion and Outlook

In this thesis we developed the theoretical foundation for blind dribbling with an intrinsically elastic robot. We derived models with different degrees of freedom of which each captures different aspects significant for achieving stable dribbling. For the one-degree-of-freedom model we obtained the analytic solution for a dribbling cycle and also elaborated a stability condition. An observer that is suitable to reliably estimate the ball motion even for the only partially observable cycle with force sensing only was derived. In other words, it makes it possible to dribble the ball without the need of vision information. The observer is also extended to a full DoF ball model and then used in the experiment with a full 7 DoF articulated robot arm. For the lateral adaptation motion, a PID controller is used.

In the subsequent simulations and experiments our approach is verified and a stable dribbling cycle is achieved. Overall, the robot is able to reactively adjust its lateral position and rotation such that it can cope with system errors as e.g. ball, robot and sensing uncertainties.

In the presented experiments, we did not yet include the height control and the observer for the vertical ball motion from yet. By using these features in a future work, it should be also possible to experimentally change the dribbling height online.

A further improvement could be the selection of more human like and rapidly changing excitation trajectories. This could lead to similar dynamic dribbling performance that humans are capable of.

The change of apex height and of the reference point is introduced as a slowly changing system via a PT1-element. A human, in comparison, is much more dextrous and is able to quickly change the overall dribbling behavior. To achieve such dexterity, a kind of planing feed-forward

control could be derived from the analytical solution. With this it could also be possible to achieve two handed dribbling.



Newton-Euler Method

An important part of model based control is to find sufficiently accurate models to describe the system behavior. To accomplish this, there are numerous approaches proposed in literature [SE04], [SK08] or [Sha98]. The most common method is Lagrange's second equation. Alternatively one may use D'Alembert's principle. The advantage of D'Alembert's principle is that the model can be accomplished by knowledge of the geometrical connections, the active forces and the mass and inertia properties. Hence, D'Alembert's principle is used in this thesis.

A short overview on the scheme is given for example in [SGS06]. More on this topic can be found in [SE04] or [Sha98]. The following sections are mainly related to [SE04].

A.1 Kinematics

Kinematics is used to describe the position of bodies in space. They are characterized by the relation of position, velocity and acceleration. The cause of motion is described in the dynamics section. In this thesis we assume that no deformations in the bodies take place (rigid body dynamics). This assumption is valid as the springs in the hand absorb the main part of the deformation energy applied by the bouncing ball.

A rigid body is able to move in 6 DoF, three translational and three rotational, if it is not subject to any constraints. In the next section the translational DoFs are described. Afterwards, there is a short introduction to the kinematics of rotation.

A.1.1 Translational Kinematics

In a Cartesian coordinate system $C = \{\mathbf{0}; \mathbf{e}_\alpha\}$, $\alpha \in \{x; y; z\}$ the position of a body i from a system of n_b bodies can be described by the translational vector

$${}^C \mathbf{p}_i(t) = r_{i_1}(t) \mathbf{e}_x + r_{i_2}(t) \mathbf{e}_y + r_{i_3}(t) \mathbf{e}_z, \quad i = 1(1)n_b. \quad (\text{A.1})$$

Depending on the objective a non-cartesian coordinate system C' , as e.g. cylindrical or spherical coordinates, may be used. Therefore, a position vector ${}^{C'} \mathbf{p}_i(t)$ can be introduced. The cartesian translational vector can be expressed in this coordinates as

$${}^C \mathbf{p}_i(t) = {}^C \mathbf{p}_i \left({}^{C'} \mathbf{p}_i(t) \right) = {}^C \mathbf{p}_i \left({}^{C'} \mathbf{p}_i \right), \quad i = 1(1)n_b. \quad (\text{A.2})$$

In technical systems bodies are often subject to kinematic constraints so that they have only n_f and not their full DoF available for motion. The n_q constraints can be written as algebraic, mostly nonlinear ($n_q \times 1$) vector equation in implicit or in explicit form as

$$\phi(\mathbf{x}(t)) = \mathbf{0} \quad \text{resp.} \quad \mathbf{x} = \mathbf{x}(\mathbf{q}, t), \quad (\text{A.3})$$

with \mathbf{q} as the ($n_f \times 1$) vector of generalized coordinates. These coordinates can also be brought in a relationship with the Cartesian coordinates ${}^C \mathbf{p}(\mathbf{q})$.

The velocity is defined as the derivative of the position vector \mathbf{p}_i with respect to time t as

$${}^C \mathbf{v}_i(t) = {}^C \dot{\mathbf{p}}_i(\mathbf{q}(t)) = \underbrace{\frac{\partial {}^C \mathbf{p}_i}{\partial \mathbf{q}}}_{J_{T_i}(\mathbf{q}, t)} \dot{\mathbf{q}}(t) + \underbrace{\frac{\partial {}^C \mathbf{p}_i}{\partial t}}_{\bar{\mathbf{v}}_i(\mathbf{q}, t)}, \quad i = 1(1)n_b, \quad (\text{A.4})$$

with J_{T_i} being the ($3 \times n_f$) Jacobian matrix of translation and $\bar{\mathbf{v}}_i$ as the generalized translational velocities. The second derivative of the position vector is the acceleration, described by

$${}^C \mathbf{a}_i(t) = J_{T_i}(\mathbf{q}, t) \ddot{\mathbf{q}} + \underbrace{\dot{J}_{T_i}(\mathbf{q}, t) \dot{\mathbf{q}} + \frac{d\bar{\mathbf{v}}_i}{dt}}_{\bar{\mathbf{a}}_i(\mathbf{q}, \dot{\mathbf{q}}, t)}, \quad i = 1(1)n_b, \quad (\text{A.5})$$

where $\bar{\mathbf{a}}_i$ are the generalized translational accelerations.

A.1.2 Rotational Kinematics

The rotation of the i -th rigid body can be described by the (3×3) rotation tensor ${}^C R_{C'_i}(t)$, which denotes the rotation from the Cartesian coordinate system $\{C'\}$ into $\{C\}$. The column vectors or ${}^C R_{C'_i}$ are unit

vectors that are the new directions of the rotated system $\{C'\}$ expressed in $\{C\}$. Consequently, ${}^C R_{C'_i}$ is an orthogonal tensor and its determinant equals one. Therefore ${}^C R_{C'_i}$ belongs to the special orthonormal group $SO(3)$.

The rotation tensor has nine parameters, even though only three parameters are needed to describe the complete rotation. The redundant parameters are defined by the properties of the $SO(3)$ group. Another possibility is to introduce generalized coordinates q as for the translational kinematics. Possible choices of generalized coordinates are e. g. quaternions, Rodriguez's parameters or Cardan angles.

By differentiating the rotation tensor ${}^C R_{C'_i}$, the $[3 \times 3]$ tensor of rotational velocity

$${}^C \tilde{\omega}_i(t) = {}^C \dot{R}_{C'_i}(q, \dot{q}, t) {}^C R_{C'_i}^T(q, t), \quad i = 1(1)n_p \quad (\text{A.6})$$

can be derived. This tensor has the special property that it is skew-symmetric. With the tilde operator defined in (2.35) it is possible to obtain a rotational velocity with vector characteristics

$${}^C \omega(t) = [\tilde{\omega}_{23}(t) \quad \tilde{\omega}_{31}(t) \quad \tilde{\omega}_{12}(t)]^T. \quad (\text{A.7})$$

ω may also be expanded to

$${}^C \omega(t) = J_{R_i}(q, t) \dot{q}(t) + \bar{\omega}(q, t), \quad (\text{A.8})$$

with $\bar{\omega}$ as the generalized rotational velocity and J_{R_i} as the $(3 \times n_f)$ Jacobian of rotation.

The rotational acceleration vector can be calculated by differentiating the rotational velocity vector, leading to

$${}^C \alpha(t) = J_{R_i}(q, t) \ddot{q}(t) + \underbrace{\dot{J}_{R_i}(q, t) \cdot \dot{q}(t) + \dot{\bar{\omega}}_i(q, t)}_{\bar{\alpha}_i(q, \dot{q}, t)} \quad (\text{A.9})$$

with the generalized rotational acceleration.

A.2 Dynamics

Section A.1 describes the description of rigid body motion. The cause of movement, cartesian forces f and torques τ , and the derivation of the dynamic equation of motion is described in this section. The forces f and the torques τ together are called Cartesian force-moment vector $\mathcal{F} = [f^T \tau^T]^T$, or wrench.

A.2.1 Classification of Forces

According to [SE04] forces can be classified with respect to the border of the system into internal forces \mathcal{F}_i^i and external forces \mathcal{F}_i^o . Another

possibility classifies them into active forces \mathcal{F}_i^a and reaction forces \mathcal{F}_i^r . Active forces are forces that are evoked by active elements as springs or actuators or physical effects as the force due to gravity. Reaction forces are the reactions to active forces in the joints and bearings of a system. Their values can be lumped to the $(n_q \times 1)$ vector of generalized reaction forces and torques

$$\mathcal{G}^r = [g_1 \ g_2 \ \dots \ g_{n_q}]^T. \quad (\text{A.10})$$

The direction \mathbf{n}_{ik} of a generalized reaction force g_k is always orthogonal to the possible movement direction. It can be specified with the implicit constraint equation (A.3) as

$$\mathbf{n}_{ik} = \frac{\partial \phi_k}{\partial \mathbf{x}} \frac{\partial \mathbf{x}}{\partial \mathbf{p}_i}, \quad i = 1(1)n_p, \quad k = 1(1)n_q. \quad (\text{A.11})$$

These direction vectors can be lumped together to the $(3n_p \times n_q)$ distribution matrix

$$\bar{Q} = \begin{bmatrix} \mathbf{n}_{11} & \mathbf{n}_{12} & \dots & \mathbf{n}_{1q} \\ \mathbf{n}_{21} & \mathbf{n}_{22} & \dots & \mathbf{n}_{2q} \\ \vdots & \vdots & \ddots & \vdots \\ \mathbf{n}_{p1} & \mathbf{n}_{p2} & \dots & \mathbf{n}_{pq} \end{bmatrix} = \begin{bmatrix} F_1 \\ F_2 \\ \vdots \\ F_p \end{bmatrix}. \quad (\text{A.12})$$

The reaction forces can also be written component-by-component as

$$\mathbf{f}_i^r = F_i \cdot \mathcal{G}^r, \quad i = 1(1)p. \quad (\text{A.13})$$

A.2.2 Newton-Euler Equations

The application of forces to a rigid body is described by the second law of Newton as

$$m_i {}^C \mathbf{a}_i = m_i \frac{d^C \mathbf{v}_i}{dt} = {}^C \mathbf{f}_i. \quad (\text{A.14})$$

with m_i being the mass of the i -th body. For application of torques to a body, the Euler equation

$${}^C I_{m_i} {}^C \boldsymbol{\alpha}_i + {}^C \tilde{\boldsymbol{\omega}}_i {}^C I_{m_i} {}^C \boldsymbol{\omega}_i = {}^C \boldsymbol{\tau}_i \quad (\text{A.15})$$

has to be applied as well. In (A.15) ${}^C I_{m_i}$ is the moment of inertia of the i -th body. For the Euler equations it is important with respect to which reference frame they are applied. A reasonable choice is the center of mass of the body. By applying Newton's second law and the Euler equation to a system of n_p rigid bodies and regarding equations (A.5) and (A.9) we obtain the Newton-Euler equations

$$\overline{M} \ddot{\mathbf{y}} + \overline{\mathbf{q}}^c = \overline{\mathbf{q}}^e + \overline{\mathbf{Q}} \cdot \mathcal{G}^r. \quad (\text{A.16})$$

With

- $\overline{\overline{M}} = \text{diag}\{m_1 I \ m_2 I \ \dots \ m_p I \ {}^C I_1 \ \dots \ {}^C I_p\}$ as the global mass matrix,
- $\overline{J} = [J_{T_1}^T \ J_{T_2}^T \ \dots \ J_{T_p}^T \ J_{R_1}^T \ \dots \ J_{R_p}^T]^T$ as the global Jacobian matrix,
- $\overline{q}^c = \left[\mathbf{f}_1^{cT} \ \mathbf{f}_2^{cT} \ \dots \ \mathbf{f}_p^{cT} \ \boldsymbol{\tau}_1^{cT} \ \dots \ \boldsymbol{\tau}_p^{cT} \right]^T$ as the global vector of Coriolis forces,
- $\overline{q}^a = \left[\mathbf{f}_1^{aT} \ \mathbf{f}_2^{aT} \ \dots \ \mathbf{f}_p^{aT} \ \boldsymbol{\tau}_1^{aT} \ \dots \ \boldsymbol{\tau}_p^{aT} \right]^T$ as the global vector of active forces.

The equations (A.16) represents $6n_p$ coupled ordinary differential equations (ODE) for n_f generalized coordinates and n_q reaction forces. Due to their differential algebraic characteristic Newton-Euler Equations are not trivially solvable. Reducing these differential algebraic equations to a system of ordinary differential equations is done by applying D'Alembert's principle which is described in the next section.

A.2.3 D'Alembert's Principle

According to D'Alembert's principle the mechanical work of movements done by reaction forces \mathbf{f}_i^r that are compatible with the mechanical constraints equals zero [Sha98]. This yields

$$\delta W^r = \sum_{i=1}^{n_p} \mathbf{f}_i^{rT} \delta \mathbf{p}_i = 0 \quad (\text{A.17})$$

for a system of n_p bodies. (A.17) implies that the possible movement directions are always orthogonal to the reaction forces.

Inserting (A.13) into (A.17) and regarding that

$$\delta \mathbf{p}_i(\mathbf{y}) = \frac{\partial \mathbf{p}_i}{\partial \mathbf{y}} \delta \mathbf{y} = J_{T_i} \delta \mathbf{y}, \quad i = 1(1)n_p, \quad (\text{A.18})$$

(A.17) can be written as

$$\sum_{i=1}^{n_p} (F_i \mathcal{G}^r J_{T_i} \delta \mathbf{y}) = \sum_{i=1}^{n_p} \left(\mathcal{G}^{rT} F_i J_{T_i} \delta \mathbf{y} \right) = 0. \quad (\text{A.19})$$

As the generalized reaction forces \mathcal{G}^r and the virtual displacements $\delta \mathbf{y}$ do not become zero in general, the scalar product $\sum_{i=1}^{n_p} F_i J_{T_i}$ has to become zero. However this sum does not have any differences to the scalar product of the two matrices \overline{Q} (cf. eq. (A.12)) and \overline{J} (cf. eq. (A.16)). This yields to the orthogonality relation

$$\overline{Q}^T \overline{J} = \overline{J}^T \overline{Q} = 0. \quad (\text{A.20})$$

A.2.4 Equations of Motion

By applying the orthogonality relation in equation (A.20), the reaction forces in the Newton-Euler Equations can be cancelled. In order to achieve this (A.16) is multiplied from the left with \bar{J}^T . This yields to

$$M(\mathbf{y}, t)\ddot{\mathbf{y}}(t) + \mathbf{k}(\mathbf{y}, \dot{\mathbf{y}}, t) = \mathbf{q}(\mathbf{y}, \dot{\mathbf{y}}, t). \quad (\text{A.21})$$

(A.21) are n_f ODEs describing the equations of motion of concatenated rigid bodies without the unknown reaction forces. The corresponding relations are

- $M(\mathbf{y}, t) = \bar{J}^T \bar{M} \bar{J}$ as the mass, matrix,
- $\mathbf{k}(\mathbf{y}, \dot{\mathbf{y}}, t) = \bar{J}^T \bar{\mathbf{q}}^c$ as the generalized Coriolis, forces,
- $\mathbf{q}(\mathbf{y}, \dot{\mathbf{y}}, t) = \bar{J}^T \bar{\mathbf{q}}^e$ as the generalized active forces.

The application of the orthogonality relation can also yield the reaction forces. Therefore, the Newton-Euler equations are multiplied from the left with the term $\bar{Q}^T \bar{M}^{-1}$. The reaction forces equation transforms to

$$\underbrace{\bar{Q}^T \bar{M}^{-1} \bar{Q}}_{N(\mathbf{y}, t)} \mathbf{g}^r(t) = \underbrace{\bar{Q}^T \bar{M}^{-1} \bar{\mathbf{q}}^c}_{\hat{\mathbf{k}}(\mathbf{y}, \dot{\mathbf{y}}, t)} - \underbrace{\bar{Q}^T \bar{M}^{-1} \bar{\mathbf{q}}^e}_{\hat{\mathbf{q}}(\mathbf{y}, \dot{\mathbf{y}}, t)}. \quad (\text{A.22})$$

B

Solution for the Hand Contact

In Sec. 3.1 we used the analytical solution of the hand contact in the 1 DoF case. In the following we derive this. The equation of motion for the hand contact in (2.3) can be written as

$$\dot{\mathbf{z}}_B = \underbrace{\begin{bmatrix} 0 & 1 \\ -K & 0 \end{bmatrix}}_{=:A} \mathbf{z}_B + \underbrace{\begin{bmatrix} 0 \\ 1 \end{bmatrix}}_{=:b} \underbrace{(-g - K(r_B - z_0 - A \sin(\omega t + \varphi)))}_{=:u(t)} \quad (\text{B.1})$$

with $K = K_H/m_B$. The initial condition is assumed to be $\mathbf{z}_{B0} = [z_{1B0} \ z_{2B0}]^T$ at $t = 0$. The free motion of this equation is calculated as

$$\mathbf{z}_{B_{free}} = e^{At} \mathbf{z}_{B0} = \begin{bmatrix} \cos(\sqrt{K}t) & \frac{1}{\sqrt{K}} \sin(\sqrt{K}t) \\ -\sqrt{K} \sin(\sqrt{K}t) & \cos(\sqrt{K}t) \end{bmatrix} \mathbf{z}_{B0}. \quad (\text{B.2})$$

For obtaining the motion that is imposed by the input $u(t)$, we may split $u(t)$ into a constant

$$u_1 = -g - Kr_B - Kz_0 \quad (\text{B.3})$$

and a time dependent part

$$u_2(t) = -KA \sin(\omega\tau + \varphi). \quad (\text{B.4})$$

The constant part yields [Lun06a]

$$\begin{aligned} \mathbf{z}_{B_{for1}} &= \int_0^t e^{A(t-\tau)} \mathbf{b} u_1 d\tau \\ &= u_1 \begin{bmatrix} \frac{1}{K} (1 - \cos(\sqrt{K}t)) \\ \frac{1}{\sqrt{K}} \sin(\sqrt{K}t) \end{bmatrix}. \end{aligned} \quad (\text{B.5})$$

For the forced motion due to the time variant part of the input $u_2(t)$, we are only calculating the first component of the state vector, as the second component is simply the time derivative of the first. We obtain therefore [Lun06a]

$$\begin{aligned} z_{B_{for2}} &= \int_0^t e^{A(t-\tau)} \mathbf{b} u_2(\tau) d\tau \\ \Rightarrow z_{1B_{for2}} &= \int_0^t \underbrace{\sqrt{K} A \sin(\sqrt{K}(t-\tau))}_{=:f_1(t-\tau)} \underbrace{\sin(\omega\tau + \varphi)}_{=:f_2(\tau)} d\tau \end{aligned} \quad (\text{B.6})$$

which is a folding of f_1 and f_2 presentable as [Lun06a]

$$z_{1B_{for2}} = \sqrt{K} A (f_1(t-\tau) \star f_2(\tau)). \quad (\text{B.7})$$

This folding can be expressed as a multiplication in the Laplace domain[Lun06a]

$$f_1(t-\tau) \star f_2(\tau) \circ\!\!\!\rightarrow F_1(s)F_2(s) \quad (\text{B.8})$$

The Laplace transforms of these two functions f_1 and f_2 can be found in [BSMM01] as

$$f_1(t-\tau) \circ\!\!\!\rightarrow F_1(s) = \frac{\sqrt{K}}{s^2 + K}, \quad (\text{B.9})$$

$$f_2(\tau) \circ\!\!\!\rightarrow F_2(s) = \frac{\omega \cos(\varphi) + s \sin(\varphi)}{s^2 + \omega^2}. \quad (\text{B.10})$$

Therewith, we get [BSMM01]

$$Z_{1B_{for2}}(s) = F_1(s) F_2(s) \quad (\text{B.11})$$

$$= \frac{kA}{(s^2 + K)(s^2 + \omega^2)} [\omega \cos(\varphi) + s \sin(\varphi)] \quad (\text{B.12})$$

$$\begin{aligned} \downarrow \quad \downarrow \\ z_{1B_{for2}}(t) &= kA \left[\cos(\varphi) \frac{\sqrt{K} \sin(\omega t) - \omega \sin(\sqrt{K}t)}{\sqrt{K}(k - \omega^2)} \right. \\ &\quad \left. + \sin(\varphi) \frac{\cos(\omega t) - \cos(\sqrt{K}t)}{K - \omega^2} \right]. \end{aligned} \quad (\text{B.13})$$

The overall solution considering (B.2), (B.5) and (B.13) is then

$$\begin{aligned} z_B(t) &= \underbrace{\begin{bmatrix} \Phi_{11} & \Phi_{12} & \Phi_{13} & 0 \\ \Phi_{21} & \Phi_{22} & 0 & \Phi_{24} \end{bmatrix}}_{=: \Phi} \begin{bmatrix} \sin\left(\sqrt{\frac{K_H}{m_B}} t\right) \\ \cos\left(\sqrt{\frac{K_H}{m_B}} t\right) \\ \sin(\omega t + \varphi) \\ \cos(\omega t + \varphi) \end{bmatrix} \\ &\quad + \begin{bmatrix} -\frac{gm_B}{K_H} - r_B + x_{H0} \\ 0 \end{bmatrix} \end{aligned} \quad (\text{B.14})$$

with

$$\Phi_{11} = x_{B20} \sqrt{\frac{m_B}{K_H}} - \frac{\sqrt{K_H} A \omega \cos(\varphi)}{\sqrt{m_B} \left(\frac{K_H}{m_B} - \omega^2 \right)} \quad (\text{B.15})$$

$$\Phi_{12} = x_{B10} + \frac{g m_B}{K_H} + r_B - x_{H0} - \frac{K_H A \sin(\varphi)}{m_B \left(\frac{K_H}{m_B} - \omega^2 \right)} \quad (\text{B.16})$$

$$\Phi_{13} = \frac{K_H A}{m_B \left(\frac{K_H}{m_B} - \omega^2 \right)} \quad (\text{B.17})$$

$$\Phi_{21} = -\Phi_{12} \sqrt{\frac{K_H}{m_B}} \quad (\text{B.18})$$

$$\Phi_{22} = \Phi_{11} \sqrt{\frac{K_H}{m_B}} \quad (\text{B.19})$$

$$\Phi_{24} = g \Phi_{13} \omega. \quad (\text{B.20})$$

Bibliography

- [ASOH04] ALBU-SCHÄFFER, A. ; OTT, C. ; HIRZINGER, G.: A Passivity Based Cartesian Impedance Controller for Flexible Joint Robots - Part II: Full State Feedback Impedance Design and Experiments. In: *Proceedings of the IEEE International Conference on Robotics and Automation*. Barcelona, Spain, 2004, S. 2666 – 2672
- [ASOH07] ALBU-SCHÄFFER, A. ; OTT, C. ; HIRZINGER, G.: A Unified Passivity Based Control Framework for Position, Torque and Impedance Control of Flexible Joint Robots. In: *The International Journal of Robotics Research* 26 (2007), S. 23 – 39
- [BH95] BANASZUK, A. ; HAUSER, J.: Feedback linearization of transverse dynamics for periodic orbits. In: *Systems and Control Letters* 26 (1995), S. 95 – 105
- [BKK88] BÜHLER, M. ; KODITSCHKE, D. E. ; KINDLMANN, P. J.: A One Degree of Freedom Juggler in a Two Degree of Freedom Environment. In: *Proceedings of the IEEE International Workshop on Intelligent Robots*. Tokyo, Japan, 1988, S. 91 – 97
- [BMS⁺10] BÄTZ, G. ; METTIN, U. ; SCHMIDTS, A. ; SCHEINT, M. ; WOLHERR, D. ; SHIRIAEV, A. S.: Ball Dribbling with an Underactuated Continuous-Time Control Phase: Theory & Experiments. In: *Proceedings of the IEEE/RSJ International Conference on Intelligent Robots and Systems*. Taipei, Taiwan, 2010, S. 2890 – 2895
- [BSMM01] BRONSTEIN, I. N. ; SEMENDJAJEW, K. A. ; MUSIOL, G. ; MÜHLIG, H.: *Taschenbuch der Mathematik*. Frankfurt am Main, Deutschland : Harri Deutsch, 2001
- [BSWB09] BÄTZ, G. ; SOBOTKA, M. ; WOLHERR, D. ; BUSS, M.: Robot Basketball: Ball Dribbling - a modified juggling task. In: *Advances in Robotics Research*. Berlin, Germany : Springer, 2009, S. 323 – 334
- [CT99] CANUDAS-DE-WIT, C. ; TSIOTRAS, P.: Dynamic tire friction models for vehicle traction control. In: *Proceedings of the*

- IEEE Conference on Decision and Control*. Phoenix, USA, 1999, S. 3746 – 3751
- [Dra92] DRAKUNOV, S. V.: Sliding-mode observer based on equivalent control method. In: *Proceedings of the IEEE Conference on Decision and Control*. Tuscon, USA, 1992, S. 2368 – 2369
- [Fon06] FONTANELLA, J. J.: *The Physics of Basketball*. Baltimore, USA : John Hopkins University Press, 2006
- [Fé] FÉDÉRATION INTERNATIONALE DE BASKETBALL (Hrsg.): *Official Basketball Rules 2010 : Basketball Equipment*. In: Fiba.com. Stand 1. Oktober 2010. http://www.fiba.com/downloads/Rules/2010/-BasketballEquipment2010_V2.pdf, Abruf: 14. November 2010
- [GASB⁺11] GREBENSTEIN, M. ; ALBU-SCHÄFFER, A. ; BAHL, T. ; CHALON, M. ; EIBERGER, O. ; FRIEDL, W. ; GRUBER, R. ; HADDADIN, S. ; HAGN, U. ; HASLINGER, R. ; HOEPFNER, H. ; JOERG, S. ; NICKL, M. ; NOTHELFER, A. ; PETIT, F. ; REILL, J. ; SEITZ, N. ; WIMBÖCK, T. ; WOLF, S. ; WUESTHOFF, T. ; HIRZINGER, G.: *The DLR Hand Arm System*. 2011. – akzeptiert zu IEEE International Conference on Robotics and Automation, Shanghai, China
- [GF04] GROTE, K.-H. (Hrsg.) ; FELDHUSEN, J. (Hrsg.): *Dubbel : Taschenbuch für den Maschinenbau*. Berlin, Deutschland : Springer, 2004
- [Had11] HADDADIN, S.: *Towards Safe Robots : Approaching Asimov's 1st Law*. Aachen, Deutschland, Rheinisch-Westfälische Technische Hochschule Aachen, Diss., 2011
- [HC75] HUNT, K. H. ; CROSSLEY, F. R. E.: Coefficient of Restitution Interpreted as Damping in Vibroimpact. In: *Journal of Applied Mechanics* 42 (1975), S. 440 – 445
- [Hog85] HOGAN, N.: Impedance control: An approach to manipulation, Part I - Theory, Part II - Implementation, Part III - Applications. In: *ASME Journal of Dynamic Systems, Measurement and Control* 107 (1985), S. 1 – 24
- [HWWAS11] HADDADIN, S. ; WEIS, M. ; WOLF, S. ; ALBU-SCHÄFFER, A.: *Optimal Control for maximizing Link Velocity of Robotic Variable Stiffness Joints*. 2011. – akzeptiert zu IFAC World Congress, Milano, Italien

- [JR3] JR3, INC. (Hrsg.): *50m31A*. In: MseriesTechData. o.A. <http://www.jr3.com/documents/datasheets/-MSeries/50M31A3.pdf>, Abruf: 10. Februar 2011
- [Kha02] KHALIL, H. K.: *Nonlinear Systems*. New Jersey, USA : Prentice Hall, 2002
- [LLL09] LUNZE, J. (Hrsg.) ; LAMNABHI-LAGARRIQUE, F. (Hrsg.): *Handbook of Hybrid Systems Control : Theory, Tools, Applications*. New York, USA : Cambridge University Press, 2009
- [Lun06a] LUNZE, J.: *Regelungstechnik 1 : Systemtheoretische Grundlagen, Analyse und Entwurf einschleifiger Regelungen*. Berlin, Deutschland : Springer, 2006
- [Lun06b] LUNZE, J.: *Regelungstechnik 2 : Mehrgrößensysteme, Digitale Regelung*. Berlin, Deutschland : Springer, 2006
- [Lyg] LYGEROS, J.: *Lecture Notes on Hybrid Systems*. In: Automatic Control Laboratory, ETH Zurich. o.A. <http://www.cs.ucla.edu/~rupak/Courses/fall09/LygerosNotes.pdf>, Abruf: 11. November 2011
- [MMS05] MAGNUS, K. ; MÜLLER-SLANY, H. H.: *Grundlagen der Technischen Mechanik*. Wiesbaden, Deutschland : B. G. Teubner, 2005
- [MSBW10] METTIN, U. ; SHIRIAEV, A. S. ; BÄTZ, G. ; WOLHERR, D.: Ball Dribbling with an Underactuated Continuous-Time Control Phase. In: *Proceedings of the IEEE International Conference on Robotics and Automation*. Anchorage, Alaska, 2010, S. 4669 – 4674
- [OASK⁺04] OTT, C. ; ALBU-SCHÄFFER, A. ; KUGI, A. ; STRAMIGOLI, S. ; HIRZINGER, G.: A passivity Based Cartesian Impedance Controller for Flexible Joint Robots - Part I: Torque Feedback and Gravity Compensation. In: *Proceedings of the IEEE International Conference on Robotics and Automation*. New Orleans, USA, 2004, S. 2659 – 2665
- [OBN02] OKADA, M. ; BAN, S. ; NAKAMURA, Y.: Skill of Compliance with Controlled Charging/Discharging of Kinetic Energy. In: *Proceedings of the IEEE International Conference on Robotics and Automation*. Washington, USA, 2002, S. 2455 – 2460
- [Ott08] OTT, C.: *Springer Tracts in Advance Robotics*. Bd. 49: *Cartesian Impedance Control of Redundant and Flexible-Joint Robots*. Berlin, Deutschland : Springer, 2008

- [RD09] REIST, P. ; D'ANDREA, R.: Bouncing an Unconstrained Ball in Three Dimensions with a Blind Juggling Robot. In: *Proceedings of the IEEE International Conference on Robotics and Automation*. Kobe, Japan, 2009, S. 1774 – 1781
- [Riv] RIVER, Wind: *Wind River Home*, o.A. <http://www.bsdi.com>, Abruf: 10. März 2011
- [RLS07] RONSSE, R. ; LEFEVRE, P. ; SEPULCHRE, R.: Rhythmic Feedback Control of a Blind Planar Juggler. In: *IEEE Transactions on Robotics* 23 (2007), S. 790 – 802
- [SE04] SCHIEHLEN, W. ; EBERHARD, P.: *Technische Dynamik : Modelle für die Regelung und Simulation*. Wiesbaden, Deutschland : B. G. Teubner, 2004
- [SGS06] SCHIEHLEN, W. ; GUSE, N. ; SEIFRIED, R.: Multibody dynamics in computational mechanics and engineering applications. In: *Computer Methods in Applied Mechanics and Engineering* 195 (2006), S. 5509–5522
- [Sha98] SHABANA, A. A.: *Dynamics of Multibody Systems*. New York, USA : Cambridge University Press, 1998
- [SK08] SICILIANO, B. (Hrsg.) ; KHATIB, O. (Hrsg.): *Springer Handbook of Robotics*. Berlin, Deutschland : Springer, 2008
- [SNI05] SHIOKATA, D. ; NAMIKI, A. ; ISHIKAWA, M.: Robot dribbling using a high-speed multifingered hand and a high-speed vision system. In: *Proceedings of the IEEE/RSJ International Conference on Intelligent Robots and Systems*. Edmont, Kanada, 2005, S. 2097 – 2102
- [Spo87] SPONG, M.: Modeling and Control of Elastic Joint Robots. In: *IEEE Dynamic Systems, Measurement and Control* 109 (1987), S. 310 – 318
- [Sti] STILMAN, M.: *Previous projects*, o.A. <http://www.cc.gatech.edu/~mstilman/earlier.html>, Abruf: 15. Oktober 2010
- [YNT98] YAMAGUCHI, J. ; NISHINO, D. ; TAKANISHI, A.: Realization of dynamic biped walking varying joint stiffness using antagonistic driven joints. In: *Proceedings of the IEEE International Conference on Robotics and Automation*. Leuven, Belgien, 1998, S. 2022 – 2029